A Non-Rigid Registration Method for Analyzing Myocardial Wall Motion for Cardiac CT Images

Elizabeth B. Philps
Marquette University

A NON-RIGID REGISTRATION METHOD FOR ANALYZING MYOCARDIAL WALL MOTION FOR CARDIAC CT IMAGES

by

Elizabeth B. Philps, B.S.

A Thesis submitted to the Faculty of the Graduate School,
Marquette University,
in Partial Fulfillment of the Requirements for the Degree of
Master of Science

Milwaukee, Wisconsin

May 2010

ABSTRACT
A NON-RIGID REGISTRATION METHOD FOR ANALYZING MYOCARDIAL WALL MOTION FOR CARDIAC CT IMAGES

Elizabeth B. Philps, B.S.

Marquette University, 2010

Cardiac resynchronization therapy (CRT) has a high percentage of non-responders. Successfully locating the optimal location for CRT lead placement on a priori images can increase efficiency in procedural preparation and execution and could potentially increase the rate of CRT responders.

Registration has been used in the past to assess the motion of medical images. Specifically, one method of non-rigid registration has been utilized to assess the motion of left ventricular MR cardiac images. As CT imaging is often performed as part of resynchronization treatment planning and is a fast and accessible means of imaging, extending this registration method to assessing left ventricular motion of CT images could provide another means of reproducible contractility assessment.

This thesis investigates the use of non-rigid registration to evaluate the myocardium motion in multi-phase multi-slice computed tomography (MSCT) cardiac imaging for the evaluation of mechanical contraction of the left ventricle.

ACKNOWLEDGEMENTS

Elizabeth B. Philps, B.S.

I would like to thank the following people for their assistance and support over the last few years. First and foremost, I'd like to thank my thesis advisor, Taly Gilat-Schmidt, for her patience and professionalism while I worked to complete coursework and thesis research while also committed to my full-time job and beginning of a family of my own.

I'd also like to thank all those people at my place of work that have provided support, research insight and encouragement, Melissa Vass and Sarah Burleton. Their support often helped to keep the balance in my life that has allowed me to maintain my sanity.

Of course, with all those who have been patient in the pursuit of my career, degree, and family, is my husband, Jason. His calming influence and endless willingness to listen to my successes and frustrations is invaluable.

TABLE OF CONTENTS

TABLE OF FIGURES

ACRONYMS

2D
Two Dimensional
Having two dimensional geometry; flat; characterized by Cartesian (x, y) coordinates

3D
Three Dimensional
Having three dimensional geometry; characterized by Cartesian (x, y, z) coordinates

4D
Four Dimensional
Characterized by Cartesian (x, y, z) coordinates and a dimension of time

AHA
American Heart Association

BiV
Bi-Ventricular

CAC
Cardiac Angiographic Catheterization

CRT
Cardiac Resynchronization Therapy

CT
Computed Tomography

DOE
Design of Experiements

ECG
Electrocardiogram

ED
End Diastole

EF
Ejection Fraction

ES
End Systole

GE
General Electric

IV
Inter-Venous

IRB
Institutional Review Board

LBBB
Left Bundle Branch Blockage

LV
Left Ventricle

MI
Mutual Information

MR/MRI
Magnetic Resonance Imaging

MSCT
Multi-Slice Computed Tomography

NYHA
New York Heart Association

PET
Positron Emission Tomography

RMS
Root Mean Squared Error

SAD
Summed of Absolute Difference

SSD
Summed of Squared Difference

TDI
Tissue Doppler Imaging

USD
United States Dollar

VTK
Visualization Toolkit

VWMS
Visual Wall Motion Scoring

GLOSSARY

akinesia
A lack of myocardial wall motion.

dyskinesia
Fragmented or jerky myocardial wall motion.

hypokinesis
Slow or diminished myocardial wall motion.

QRS
The region of an electrocardiogram that signifies the depolarization of the cardiac ventricles.

TABLE OF DATASETS

Synthetic Dataset A

Description: Elliptical synthetic data. Intensities increase from the center of the ellipse outward. The synthetic ellipse object was defined over 121x121x121 voxels with a dynamic range of approximately 4400 intensities.

Synthetic Dataset B

Description: This dataset was created by applying a known transformation to Synthetic Dataset A. The prescribed transformation involves increasing radial motion from the center of the ellipse outward.

Synthetic Dataset C

Description: This will be used to refer to an image series created from registering Synthetic Dataset A to Synthetic Dataset B.

Clinical Dataset X

Description: A patient clinical image series with normal left ventricle function. The image series consisted of volumetric reconstructions at 10 cardiac phases.

Clinical Dataset Y

Description: This will be used to refer to the image series created from registering the systole to diastole image phases of Clinical Dataset X.

Clinical Dataset Z

Description: A patient clinical image series with known pathology. The image series consisted of volumetric reconstructions at 20 cardiac phases.

CHAPTER 1 INTRODUCTION

1.1 Problem Statement

Heart failure afflicts approximately 5 million Americans, resulting in 300,000 annual deaths.[4] Cardiac resynchronization therapy (CRT) is a used to treat heart failure due to cardiac dyssnchrony, for example myocardial conduction system delay due to left bundle-branch blockage. The effectiveness of CRT is limited, as the procedure has a high percentage of non-responders (~30-50%).[41]

Successfully locating the optimal location for CRT lead placement on a priori images can increase efficiency in procedural preparation and execution and could potentially increase the rate of CRT responders. Recent studies suggested that improved pacing is possible by placing a pacing lead at the site of the most delayed mechanical motion.[47] Therefore, identifying the site of the most delayed region prior to lead placement is an ongoing challenge. To address this challenge, previous work implemented registration algorithms for cardiac MR and developed statistical models for identifying regions of abnormal wall motion. While promising, MR acquisitions are not routinely prescribed prior to CRT, due partly to issues of cost. As CT imaging is often performed as part of resynchronization treatment planning and is a fast and accessible means of imaging, developing a registration method for assessing left ventricular motion of CT images could be beneficial. Automated 3D ventricular motion analysis utilizing registration and motion transformation evaluation can provide an objective and

reproducible means to perform assessment that is currently performed manually on 2D images, which causes increased inter- and intra-observer variability. [73]

This thesis investigates the use of a 3D non-rigid registration to evaluate the myocardium motion in multi-phase multi-slice computed tomography (MSCT) cardiac imaging for the evaluation of mechanical contraction of the left ventricle.

1.2 Project Objectives

1.2.1 Non-Rigid Registration

The first objective of this thesis was to develop and validate a 3D non-rigid registration technique to extract the motion transformation of a multi-phase CT image series. Chapter 3 summarizes the algorithm design and describes the techniques implemented to validate and optimize the algorithm performance including (1) the development of a synthetic data series to mimic clinical cardiac images, (2) a design of experiments to select optimal algorithm parameters, and (3) the results of the design of experiments applied to the synthetic images and to clinical cardiac images.

1.2.2 Motion Analysis

The second objective of this thesis was to apply the developed algorithm to clinical CT time-series datasets. A preliminary comparison of the transformations obtained from the non-rigid registration of a normal and pathological dataset was performed to evaluate whether the resulting motion data may be beneficial for analyzing wall motion characteristics. Chapter 4 summarizes the evaluation of the motion transformation obtained from the non-rigid registrations of both a normal and

pathological clinical data series. Motion vectors were plotted for both clinical series and compared to determine similarities and differences between the motion.

CHAPTER 2 BACKGROUND

2.1 Background

2.1.1 Heart Failure: An Epidemic

Cardiovascular disease is one of the leading causes of morbidity and mortality in Western civilization, especially the United States.[1,2,3] Increased survival rates of myocardial infarction due to improved medical and surgical interventions and thrombolytic therapies have led to a growing elderly population.[75] Consequently, the increasing population of patients surviving with reduced cardiac function contributes to an increased economical burden on health services from the high costs of longer-term drug therapies and hospitalization.[2] Approximately 5 million individuals in the United States are afflicted by heart failure and nearly 300,000 deaths result each year from heart failure and related complications of the disease. On average, $6,000 USD are spent on an annual basis per patient case of cardiac failure.[4] For these reasons, earlier and more effective treatments are needed to reverse the effects and minimize the costs of medical care needed for treatment of chronic heart failure.

In recent years the epidemiology of coronary heart disease has advanced, whereas that of heart failure caused by other related cardiac factors is less well known. Sudden cardiac death has demonstrated recent decline since the early 1980s, mainly due to the decline in coronary heart disease.[5,6] Increases in the incidence of congestive heart failure, however, are expected to combat this decline. [6]

There are several variations on the definition of chronic heart failure.[7,8] One general definition of heart failure is "a pathophysiological state in which an abnormality of cardiac function is responsible for the failure of the heart to pump blood at a rate commensurate with the requirements of the metabolizing tissues."[7] This generalized definition suggests that heart failure is characterized by a reduction in the ejection volume of each cardiac stroke, leading to a reduction in left ventricular contraction efficiency and the reduction of the systolic function despite the same amount of energy exerted to contract the muscle. The New York Heart Association (NYHA) classifies heart failure by levels of patient activity:[7]

Almost 20% of patients with myocardial failure die within 1 year of initial diagnosis of the disease; this accounts for a greater than 80% eight-year mortality rate. Fifty percent of these deaths are sudden, suggesting heart failure patients are 6-9 times more likely to suffer sudden cardiac death than individuals of the general population.[9,10]

2.1.2 Heart Failure Causes

Chronic heart failure may result from one or a combination of factors including, but not limited to, myocardial ischemia, myocardial dysfunction, cardiac arrhythmia, valvular anomalies, pericardial diseases, or rhythm disturbances. Valvular anomalies, for example, impede the activation of the papillary muscles responsible for the opening and closing of the mitral valves; this complicates cardiac hemodynamics and reduces the rate at which the heart can mechanically transport blood to the systemic system. [11] Other factors, although less commonly the causes of heart failure, may worsen the status of the heart failure such as anemia, renal or thyroid dysfunctions, or cardiodepressant drugs. [7]

Figure 1: New York Association (NYHA) Classification of Heart Failure[7]

* Class I: patients with no limitation of activities; they suffer no symptoms from ordinary activities.
* Class II: patients with slight, mild limitation of activity; they are comfortable with rest or with mild exertion.
* Class III: patients with marked limitation of activity; they are comfortable only at rest.
* Class IV: patients who should be at complete rest, confined to bed or chair; any physical activity brings on discomfort and symptoms occur at rest.

As the survival rate of myocardial infarction increases, more individuals are living with reduced ventricular function, which may result in eventual heart failure. For

patients with asymptomatic left ventricular dysfunction, well-defined strategies for preventing myocardial and ventricular remodeling are necessary. [4]

This thesis will emphasize the 20 to 30% of New York Heart Association (NYHA) patients of classes III-IV heart failure manifested most frequently as left bundle branch blockage (LBBB). [12] Bundle branch blockage (BBB) results in contractile inefficiency and dyssynchrony (either *atrioventricular*, being dyssychrony between the atrial and ventricular contractions, or *intraventricular*, being dyssychrony between the left and right ventricular contractions), with consequences of further reduction in ventricular function. Both atrioventricular and intraventricular conduction disorders contribute to heart failure associated with ischemic and *idiopathic* (cause unknown) dilated *cardiomyopathy* (enlargement of ventricle resulting in reduced pumping efficiency). [13] The conduction delays imposed by LBBB lead to asynchrony inducing hemodynamic changes and alterations in systolic and diastolic function. [14] Conduction pathways for normal ventricular function are known, but the abnormalities and variations associated with BBB have not been adequately characterized. The extent and implications of the impulse conduction delay within the heart, both atrioventricular and intraventricular, is not fully understood.

2.1.3 Heart Failure Diagnosis

The most common precursors and symptoms of chronic heart failure include coronary artery disease, chronic hypertension, cardiomyopathy, valvular dysfunction, cardiac arrhythmia and conduction disturbance (electrophysiology), pericardial disease, and infection. [15] Effective identification of the symptoms and signs of heart failure are

the first step to proper treatment, but no single investigation can be considered the "gold standard" for the confirmation of the clinical diagnosis of heart failure.[2] Currently, although electrocardiography has been utilized to aide in the diagnosis of LBBB, few studies also include the complimentary investigations of coronary angiography, left ventriculography, and hemodynamics to fully characterize the disease.[16] WJ Remme and K Swedberg from the Task Force for the Diagnosis and Treatment of Chronic Heart Failure have concisely outlined the algorithm for which to guide in the proper diagnosis of heart failure utilizing several investigatory techniques.[7] The algorithm, featured in Figure 2, demonstrates that a combination of multiple diagnostic tools is necessary for proper characterization of the disease.

Figure 2: Algorithm for Diagnosis of Heart Failure[7]
This figure demonstrates the steps typically taken to strategically diagnose heart failure.

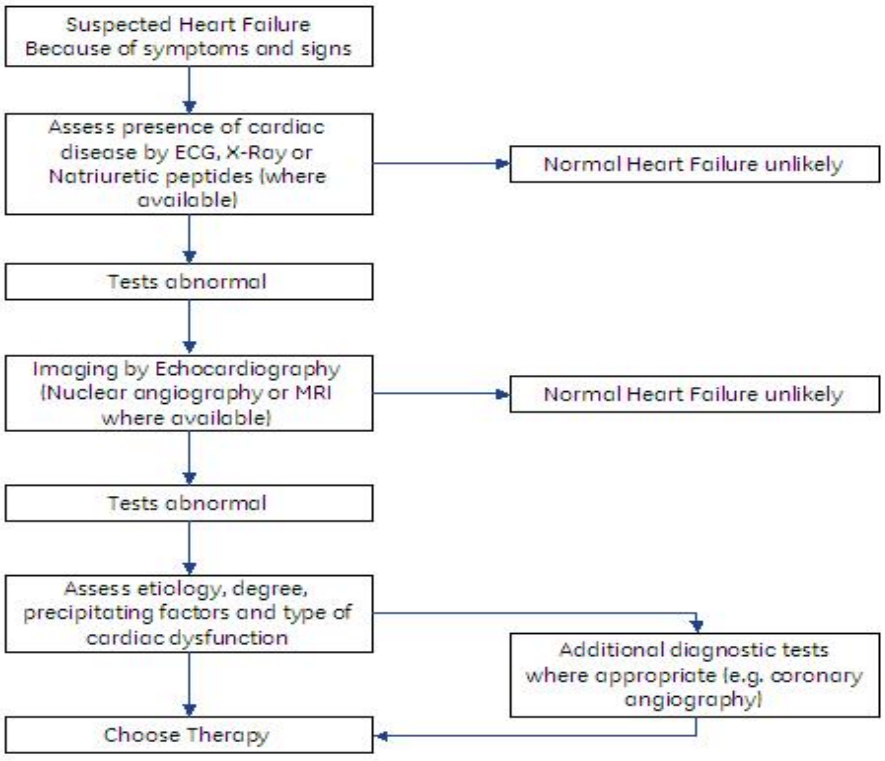

Diagnosis is based on a combination of patient history, clinical examinations, physiological testing, electrocardiography, biochemical assays, and imaging studies. [17] Prognosis of congestive heart failure can be further determined through peak oxygen uptake values, left ventricular ejection fraction (LVEF), signal-averaged electrocardiography (ECG), and electrophysiologic testing. [3] Many different imaging modalities are used in the diagnosis and treatment planning of heart failure, such as x-ray, echocardiography, nuclear medicine and magnetic resonance imaging. For a comprehensive evaluation of the heart, an imaging modality should provide the following: a high spatial resolution for proper anatomical assessment, the detection and quantification of stenotic lesions in the coronary arteries, possible evaluation of LV contractility, the detection of abnormal blood flow, and the detection of myocardial viability. [18]

Computed Tomography (CT)

The gold standard for assessment of left ventricular ejection fraction continues to be ultrasound echocardiography, although the temporal and spatial resolutions of both magnetic resonance imaging (MRI) and computed tomography (CT) are improving to provide more accurate results. [18,19,20] Developments in the accuracy and consistency of CT have significantly improved the morphological, functional, and vascular information that can be obtained from a CT cardiac examination. [18] ECG synchronization with the CT image acquisition provides detail to delineate images from different segments of the ECG cycle, for example the phases of end-diastole and end-systole. Cardiac CT has a

variety of applications. A majority of these are solely to evaluate anatomical aspects of the heart, but other applications that contribute to the functional aspects of the heart are also being investigated, for example myocardial perfusion. [18] Anatomical assessments include calcium scoring and other coronary artery assessment, morphological analysis, ventricular function, vessel run-off, and treatment follow-up. [18]

In general, the procedure for performing a CT acquisition involves the IV administration of a contrast agent to the patient to enhance the cardiac vasculature for optimal vessel opacification and a series of short x-ray exposures to localize anatomy, optimize contrast timing, and acquire multi-phase data at applicable time periods of the ECG cycle. With more recent technology and the introduction of 64-slice and greater scanners, these types of CT cardiac scans are acquired in as short as 20 seconds. [21] CT cardiac exams can be acquired in one of two modes, "prospectively" gated and "retrospectively" gated. In prospectively gated acquisitions, x-ray output is pulsed to acquire axial images at pre-determined ECG time intervals. In retrospectively gated acquisitions, a helical (or spiral) acquisition involving continuous table movement is used to acquire cardiac images simultaneously with an ECG signal acquisition and recording; views are then retrospectively sorted and reconstructed at the desired intervals of the cardiac cycle. [18]

One specific application of anatomic cardiac CT is pre-operative planning of electrophysiology interventions. Visual assessment of CT images for the localization of pulmonary veins prior to ablation of the heart muscle in the treatment of atrial fibrillation is essential to proper planning of percutaneous radiofrequency ablation catheter placement. [21] Variations in pulmonary veins are common and proper placement planning

of ablation seeds is necessary to provide familiarity to the physician prior to the procedure to assure the therapy is provided as accurately as possible. CT images provide the tools for accurate localization planning of these procedures with minimized effects to normal surrounding tissues.

Ventricular functional analysis is used for the visualization and quantification of different phases of the cardiac cycle and at different stress levels. Both the global indices of cardiac function, such as stroke volume, ejection fraction, and cardiac output, and the local indices of cardiac function, such as wall thinning and thickening, can be obtained from CT images.[22] From CT multi-phase datasets, regional wall motion can be evaluated by visual ranking of dyskinesia and akinesia of certain segments of the heart wall.[23] More sophisticated functional analysis, whether global or local, may require segmentation of the epi- and endocardial boundaries of the cardiac muscle, most often the left ventricle. Segmentation of these boundaries is used to determine the volumes and the motion characteristics of the ventricle on a more objective quantitative level. Boundaries of these volumes can be determined manually by the operator[24] or semi-automatically or automatically using software algorithms to detect the ventricle contours.[25]

New advancements in CT are also being made to extend the capabilities of this imaging modality beyond anatomical-only analysis into the realm of functional analysis. Investigations are being made into using contrast-enhanced CT to assess myocardial perfusion and viability with early and late contrast enhancement protocols.[26] Similar to recent MRI techniques, CT techniques are being evaluated that demonstrate microvascular occlusion on late perfusion images of individuals with re-perfused acute infarcts.[27] These techniques involve well-timed imaging of the myocardial during first-

pass imaging (as the contrast agent first flows through the ventricle) and during late enhancement periods (as the contrast agent has had time to transfer into the myocardial muscle tissue). These studies of myocardial perfusion and viability present similar information as from nuclear medicine perfusion and viability scans pertaining to the blood flow capabilities and the metabolic functionality of the myocardial muscle tissue.

ECG

One of the less invasive investigations, electrocardiography, aides in the assessment of the electrical impulses of the heart, which, in patients with LBBB, most often demonstrates a prolonged QRS duration.[16] Figure 3 below shows a typical, normal physiological electrocardiogram waveform as read on the right arm to left leg lead voltages.

Figure 3: Typical Echocardiogram

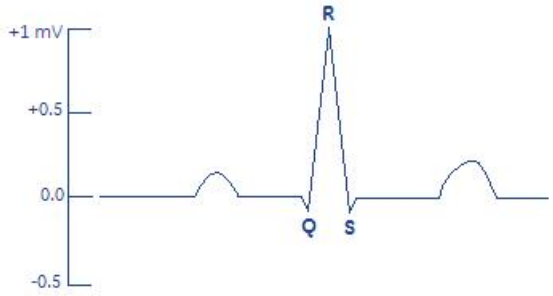

The QRS complex of a normal ECG heart cycle waveform represents the depolarization of the ventricular muscle cells, typically lasting between 60 and 100 milliseconds. Atrial cell repolarization often occurs during this same period, but this signal is overshadowed by that of the ventricular depolarization signal.[39] Figure 4 demonstrates a typical result of an ECG for a LBBB patient. Activation from the

atrioventricular node cannot effectively be sent through the left bundle-branch of the heart, and, therefore, the electrical impulse does not travel through the left ventricle directly, but only by proceeding first through the right ventricle, then to the left ventricle. This inefficient transfer from the right ventricle through the intraventricular septum and, eventually, to the left ventricular muscle causes a delay in the QRS complex of the ECG trace by $\geq$ 0.12 seconds. This contributes to a very broad S wave in ECG leads V1 and V2 and broad R wave in V5 and V6, as demonstrated in Figure 4. [40]

Figure 4: LBBB QRS Duration and Associated Cardiac Electrical Propagation[40]

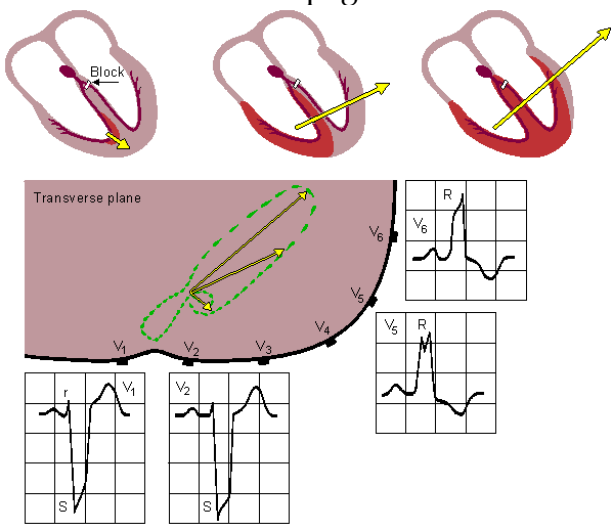

X-RAY

X-ray angiographic catheterization also plays a large role in the evaluation of a variety of heart failure precursors, most prevalently, coronary artery disease and electrophysiology. Cardiac angiographic catheterization (CAC) is a clinical gold standard for assessment of coronary disease, providing accurate depictions of coronary artery stenosis and occlusion. This modality also provides a means for physicians to deploy specialized catheters to different locations of the heart to assess the electrical impulses and pathways and a similar deployment method is used to deliver cardiac

resynchronization therapies in the form of cardiac pacing directly to the muscles of the heart.

Multiple imaging modalities are pertinent in the diagnosis of heart failure, as described above. Another goal of imaging techniques is to provide a more accurate depiction of how to tailor treatments and therapies of heart failure to the needs of each individual patient.

2.1.4 Treatments

Ultimate aims of chronic heart failure treatments are shown in the following figure. [7,12]

Figure 5: Aims of Treatment of Chronic Heart Failure[7]

1. Prevention
(a) Prevention and/or controlling of diseases leading to cardiac
dysfunction and heart failure
(b) Prevention of progression to heart failure once cardiac
dysfunction is established
2. Morbidity
Maintenance or improvement in quality of life
3. Mortality
Increased duration of life

Any treatment methods deployed to treat chronic heart failure must control the disease from further dysfunction of the heart's mechanical capabilities, they must not reduce the quality of life of the individual, and they must have a positive increase in the duration of the life of the afflicted individual. Once myocardial dysfunction is present, the cause of the dysfunction must first be removed or reduced as much as possible. Causes of ventricular dysfunction may include ischemia, alcohol, drugs, or, in some cases, thyroid disease. Once the present underlying cause has been removed, therapy must be deployed to reduce any progression from the current state of dysfunction to chronic heart failure. [7]

One method of treatment of cardiac dyssynchrony, known as cardiac resynchronization therapy (CRT), is applicable to patients with myocardial conduction system delay, often manifest as left bundle branch blockage (LBBB). [12] This nonpharmacologic therapy is assumed to correct the electrical component of the underlying electromechanical delay in the left and right ventricular activation, thus counterbalancing the delay in activation of the left ventricle caused by LBBB. [41] There are convincing results that demonstrate the positive effects of biventricular pacing (one specific method of CRT) including an increase in the left ventricular ejection fraction, a decrease in mitral regurgitation, and an improvement in other related symptoms of heart failure. [41,42] Two main mechanisms are vital to the therapy of this type of heart failure, as proposed by Ansalone et al., (1) an increase in preload after the optimization of the atrioventricular delay with right sequential pacing, and (2) cardiac resynchronization with biventricular (BiV) pacing in patients with left ventricular (LV) asynchrony caused by LBBB.[42] CRT has been evaluated in many trials and has shown positive effects such as

improved quality of life, improved exercise capacities, and improved left ventricular functional parameters.[42] The MIRACLE trial (mutlicenter InSync randomized clinical evaluation) was one of these trials, in which a large placebo controlled trial confirmed the beneficial effects of CRT. In 2002, biventricular cardiac resynchronization therapy (BiV-CRT) was supplemented to the American Heart Associations guidelines for Pacing and Electrophysiology[42], which indicate that BiV-CRT be limited to patients with drug refractory, symptomatic NYHA classes III-IV with a prolonged QRS ECG, LV end diastolic (ED) diameter greater than 55mm, and LV ejection fraction (EF) less than 35%.

CRT Procedure

During a cardiac catheterization procedure, pacemaker leads are introduced into the body via a vein in the chest and snaked up through the main blood vessels to reach the heart. The pacemaker leads are then navigated to the right ventricle and also into the coronary sinus vein. Three leads are implanted in total - one to regulate the right ventricle, one to regulate the left ventricle (via implantation in the coronary sinus), and one to regulate the right atrium (near the sinoatrial node). From these locations, the pacemaker device can sense the heart's electrical impulses as well as send impulses to synchronize the leads as specified by the clinician. The leads can be programmed to send an electrical impulse at specified time intervals. In patients with chronic heart failure due to LBBB, both interventricular dyssynchrony and intraventricular dyssynchrony can be managed by selecting an ideal timing of pacing impulses between right and left ventricular activation.[43]

Improved Diagnosis and Treatment

Cardiac resynchronization therapy has a high percentage of nonresponders - as high as 30-50% of heart failure patients with LBBB. [41] Reducing the number of nonresponders or, at minimum, identifying and characterizing the nonresponders apart from the positive responders can contribute to personalized cardiac resynchronization therapies for responders and to determining an alternative therapy or optimized resynchronization therapy for nonresponders.

Many factors may contribute to the significantly large category of nonresponders including suboptimal simultaneous activation of each of the right and left ventricular walls. Other variables contribute to the lower than desired percentage of positive responders to resynchronization therapy, among these are pacing lead placement sites, conduction delay intervals, and appropriate tradeoff between atrioventricular timing optimization. [43,44] Proper placement of the left ventricular pacemaker lead is key for successful resynchronization of the electrical and resulting mechanical activation of the left ventricle. The activation of the left ventricle is necessary for ventricular systole for optimal contraction and efficiency of the heart. Typically, this lead is placed at the free wall of the LV, consistent with the location of the lateral cardiac vein of the coronary sinus. [44] This site was shown to provide positive results in cardiac contractility for BiV patients as per the work of Auricchio et al. [45,46] Further study suggested that anterior or anterolaterial wall positioning provided superior LV ejection fraction and NYHA functional classification over positioning in lateral or posterolateral lead placement. [43] More recently, a Tissue Doppler study by Ansalone et al. demonstrated positive results with lead placement at the site of most delayed mechanical contraction, often times being

the lateral wall, but not in all cases.[47] These findings support the hypothesis that the anatomical lateral wall may not be optimal for every patient, being that not every patient's cardiac anatomy and pathophysiology is the same from one case of LBBB to the next.[47] Heart failure patients often die prematurely despite the attempts to provide an "optimal" therapy. CRT is seen as currently addressing the need for improving heart failure therapy,[12] bringing electrophysiologists and pharmacotherapists together to treat the debilitating disease. However, improved methods of delivery and therapy optimization of ventricular synchronization is key for further development.

Further optimization of the placement of biventricular lead placements can, theoretically, continue to improve the mechanical parameters of heart failure patients. Currently, assessment of the mechanical status of the heart for determination of lead placement is performed utilizing echocardiography and x-ray cardiac catheterization. Tissue Doppler Imaging (TDI) has been shown to be helpful in determining the severity of LV dyssynchrony and for determining the effects of different pacing on the mechanical functionality of the heart during biventricular procedures.[47,48] A standard transthoracic echocardiogram was obtained for these measurements, providing images of the heart through the chest wall to assess LV end diastolic volume (EDV), LVEDV index, LV end systolic volume (ESV), LVESV index, and LV ejection fraction (LVEF) using a modified biplane Simpson rule, a method of determining the volume of the LV using additive Riemann sum of multiple volume disks that represent small incremental portions of the LV volume.[49]

Although currently the gold standard for the diagnosis of heart failure[50] and left ventricular function analysis, echocardiography is being challenged by the functional

assessment capabilities provided by magnetic resonance imaging, nuclear medicine, and computed tomography. Whereas left ventricular functional analysis using echocardiography is based mainly on two-dimensional image analysis and is susceptible to interobserver bias and operator experience, mutli-phase computed tomography images are now used to analyze two-dimensional and three-dimensional wall-motion and function of cardiac images.[20,22,24,25,42,51] The spatial and temporal resolution of CT imaging is improving, potentially beyond that of echocardiography.[19] Although computed tomography uses ionizing radiation, it has become an integral part in pre-operative planning for cardiac catheterization electrophysiological procedures involving ablation and lead placement.[52] Therefore, more information could be extracted from these computed tomography images without necessarily imparting more dose to the patient than is already required and without additional investigatory examination.

Computed tomography images have been used to assess regional and global wall motion and estimate left ventricular functional parameters, such as end diastolic volume, end systolic volume, and ejection fraction. Mutliple methods can be used to assess these parameters, such as contour detection, segmentation, etc.[18] Rarely, however, have these methods been used to assess the global and regional mechanical delay of the left ventricular, let alone the right ventricle or left and right atrial mechanical characteristics. Assessing these parameters would allow electrophysiologists to, not only pre-operatively prepare for the specific anatomical caveats on a per patient basis, but it would allow them to pre-operatively assess the mechanical characteristics of the heart to evaluate for optimal lead placement during biventricular cardiac resynchronization therapy.

2.2 Image Registration

Image registration is the method of arranging two (or more) associated images. This work focuses on the techniques of image registration for alignment of radiological medical images. Medical image registration has proven beneficial in the diagnosis, planning, and treatment across multiple imaging modalities, across longitudinal image studies, and across normal versus pathological specimens.[65]

For the purpose of this work, image registration can be used to align two images from the same patient at different time points. Registering images to a common coordinate system, perhaps a reference anatomical model, can facilitate the analysis of correlate anatomy and function of that anatomy. In addition to these methods, image registration can be extended to the characterization and compensation of movement of a target anatomy, such as the analysis of perfusion image of the heart to compensate for patient respiration.[66]

Registration applies to both spatial and temporal registration of images. Rather than images of different coordinate systems, these methods consider images of the same coordinate system at different image time points.

There are three fundamental steps to a registration method, including (1) the transformation model that defines the method in which one image is altered to correspond to the other image, (2) the similarity measure that reports the level of semblance between the images (before, during and/or after transformation of the images), and (3) the optimization process that alters the transformation metrics to produce the most desired similarity results. Each of these components must be considered in the utilization of a registration algorithm for medical image alignment.

2.2.1 Image Transformations

The first fundamental constituent of image registration is the transformation technique, which describes how one image (often referred to as the source image) will be altered to correspond more to the second image (referred to as the target image). In other words, the transformation describes in what manner the voxels of the source image can be deformed to better match the target image. There are, generally, three classes of transformations: rigid transformations, affine transformations, and non-rigid transformations. Depending on the type of medical images being analyzed or the type of information desired from the registration of the images, each of these classes provides different benefits.

2.2.1.1 Rigid Transformations

Rigid transformation of a 3D medical image allows for only six degrees of freedom (DOFs), namely translational movement in the x, y, and z directions and rotational movement about the three axes. These types of transformations ensure that each voxel within the image preserves the same distance between all points after transformation as were defined before transformation. Rigid transformation is selected for registration of anatomy that experiences only rigid motion between source and target images. Bony structures and relatively stationary organs can often be registered successfully between scans of the same patient, as these structures do not undergo significant structural compression or gross physiological motion, and remain structural consistent. [65]

2.2.1.2 Affine Transformations

Like rigid transformations, affine transformations allow for the same 6 degrees of freedom, but additionally provide 3 scaling and 3 shearing directional parameters – yielding twelve total DOFs. Affine transformations preserve parallel lines after transformation but not necessarily the length of the lines or the angles between lines. These types of transformation are best utilized in medical applications where geometric distortion appears in the form of scaling or shearing. An example of this may be longitudinal imaging studies of a pediatric anatomical study in which the patient's anatomy is the same but scaled through years of aging. Affine transformation is also considered more accurate type of transformation for intersubject registration to account for similar anatomy of different size in different subjects. [65]

2.2.1.3 Non-rigid Transformations

Depending on the non-rigid transformation method used, the number of DOFs far outnumbers those of rigid or affine transformations. Subsequently, this requires increased computation cost over the other transformation methods. These types of transformations are commonly used when local changes occur between the images of interest, such as soft tissue deformable structures within a subject or across subjects. [65] For the purposes of this paper, for example, non-rigid registration will be applied to assess the deformation of the cardiac motion throughout the cardiac cycle within an intrasubject computed tomography (CT) image acquisition.

Several non-linear transformation models exist that have been applied to medical imaging, including elastic, fluid, and spline models of registration. These methods have been surveyed and summarized by Daniel Rueckert.[65] A brief explanation of each group will be provided below as well as a justification for utilization of each model for different applications.

2.2.1.4 Elastic and Fluid Transformations

First proposed by Bajcsy et al. in 1989[71] an elastic model can be described as the transformation of a source image into the target image in a physical process that models the stretching of an elastic material, such as rubber. Two forces, an internal and an external force govern the transformation. The external forces act to deform the elastic (rubber) physical body, and the internal force (internal stresses) act to maintain a smoothness constraint on the body. Deformation ceases when both forces arrive at an equilibrium state. These methods were initially suggested for registering CT human brain images to a brain atlas. Elastic transformations, however, are limited in that profoundly localized deformations are not easily modeled. This is caused by the fact that deformation energy caused by the internal forces increases directly with the strength of the deformation. Fluid registration, on the other hand, allows for an approach in which the stresses relax with deformation over time.[65] This makes fluid deformation more suitable for intersubject registration. This method of registration, however, allows for concentrated local deformations but also poses a potential increase in misregistration as fluid transformations involve a large number of DOFs.

2.2.1.5 Spline

The concept of splines originates from long flexible materials used to model surfaces of large machinery. Spline transformation is based on the principle that conceptual splines can be used to model a transformation of one image into another. In this model, a set of corresponding points, called control points, are defined both within the source and target images. In this way, spline based registration assumes that these set of corresponding landmarks, or control points, can be found in both images. A spline-based transformation approximates the movements necessary to map each source image control point to the corresponding control point within the target image. A smoothness parameter was enlisted to ensure displacements occurs seamlessly between these landmarks in the work of Goshtasby.[67] Meyer et al.,[69] further proposed revising the landmark locations based on voxel intensity similarity measures, and Davis et al. in 1997[70] further extended spline transformations to include control points arranged with equidistant spacing throughout the image, forming a control point mesh as opposed to relying on anatomical or geometrical landmark locations. These mesh grids of control points are often referred to as pseudo- or quasi- landmarks.

One specific type of spline, thin-plate splines, utilizes transformations to map an original image, modeled as a flat metal sheet, to its target image with in-plane bending only. Each displacement in the plate, however, has a global influence on the transformation, thus problematic in attempting to evaluate local deformations. An alternative spline method is based upon free-form deformations utilizing B-splines. Although thin-plate splines provide for a method of manipulating an arbitrary configuration of control points, B-spline deformation requires a mesh of uniformly

spaced control points. This method was first suggested by Reuckert et al. in 1999 to register contrast enhanced MR mammography images.[68] B-splines involve deformation that controls the shape of the 3D object, ensuring a smooth and continuous transformation. In this method, the effect of changing localized control points is limited to the neighborhood of each control point, providing recovery of deformations in the vicinity of the respective control point. The smooth and continuous transitions allow for effective transformation of control point motion over time. In addition to the fact that these algorithms are readily available, B-splines have wide general applicability and computational efficiency.[65] At very fine resolutions, however, folding of the deformations field becomes possible and special measures are required to prevent these disadvantages. [65]

2.2.2 Similarity Metrics

Medical image registration is often categorized as utilizing either geometric or intensity similarity approaches. For the purpose of this investigation, the geometric approaches, such as point-based and surface-based similarity metrics will not be discussed in detail. Voxel intensity-based approaches will be the focus of this thesis, particularly mutual information, as they have become, in recent years, robust and accurate enough to use target and source image intensities without image segmentation or delineation of corresponding structures.[65] These methods also contain an advantage in that they do not require image feature, such as surface or 3D volume, extraction. Voxel intensity approaches assume that the target and source images are most similar at the optimal registration between the two images.

Perhaps the simplest voxel intensity similarity measure that can be implemented is sum of squared differences, also known as sum of squared error, presented in Figure 6 below.[66]

Figure 6: Equation for SSD[65]

$$SSD = \frac{1}{N_{x_A}} \sum_{\in \Omega_{A,B}^{T}} | A(x_A) - B^T(x_A) |^2$$

where x_A denotes the voxel locations, A and B are the untransformed images, T represents the transformation operation, $\Omega_{A,B}^{T}$ is the overlapping domain between the images, and N is the number of voxels within the overlapping domain.

This technique assumes that the target and source image intensities are identical at final registration, excluding noise characteristics. Because SSD is the optimal similarity measure for images that only differ by Gaussian noise, SSD is appropriate for registration between images of the same imaging modality, for example CT to CT or PET to PET, but is not even always ideal for intramodality imaging.[66] The smallest SSD provides the best alignment; therefore, as the value of SSD decreased, the alignment is improved.

As the equation shows, corresponding intensities within the images are subtracted from each other to obtain the difference and then squared. Whereas SSD can be skewed by large intensity differences between only a few image voxels, the sum of absolute differences (SAD) measure is less sensitive to these outlying voxels. The calculation of SAD minimizes the effect of those problematic voxel differences by removing the squared effects.[65] The equation for SAD is provided in Figure 7.

Figure 7: Equation for SAD[65]

$$SAD = \frac{1}{N_{x_A}} \sum_{\in \Omega_{A,B}^T} | A(x_A) - B^T(x_A) |$$

This method, for example, is useful if contrast media is injected into the organ of interest between the acquisition of the target and source images. Contrast injection can cause large intensity differences at corresponding landmarks, which will be minimized using a SAD technique over an SSD technique.

Another voxel-based similarity metric is the correlation coefficient. This method assumes a linear relationship between the target and source image intensities. Similarly to SSD, correlation coefficient based metrics are optimized for intramodality registration.[66] Figure 8 defines the equation for correlation coefficient.

Figure 8: Equation for Correlation Coefficient[65]

$$CC = \frac{\sum_{x_A \in \Omega_{A,B}^T} (A(x_A) - \overline{A}) \cdot (B^T(x_A) - \overline{B})}{\{\sum_{x_A \in \Omega_{A,B}^T} (A(x_A) - \overline{A})^2 \cdot \sum_{x_A \in \Omega_{A,B}^T} (B^T(x_A) - \overline{B})^2\}^{1/2}}$$

where $\overline{A}$ is the mean voxel value in image A and $\overline{B}$ is the mean voxel value in image B.

In this approach, the source image is aligned with the target image and corresponding image intensities are multiplied until the maximum correlation coefficient is obtained.[65]

The correlation coefficient metric is a normalized version of the cross correlation measure shown in Figure 9.

Figure 9: Equation for Cross Correlation[65]

$$CC = \frac{1}{N} \sum_{x_A \in \Omega_{A,B}^T} A(x_A) \cdot B^{\mathrm{T}}(x_A)$$

In aligning two images, one can also measure the amount of information and uncertainty provided by the combined images, as is calculated by the metric of joint entropy. If there is no commonality between the target and source images, the joint entropy equals the sum of the entropies of each respective image. As the images become more alike, the joint entropy reduces related to the sum of the individual entropies. Figure 10 is an equation that represents this relationship, with the function H representing the entropy.

Figure 10: Relationship for Commonality of Joint Entropy

$$H(A,B) \leq H(A) + H(B)$$

This equation represents the desire to have the amount of entropy in the combined images to be no more than the sum of the entropies of the individual images. Two-dimensional histograms can be used to represent the joint entropy of a pair of images, where the intensity of the voxels in A,A(x_A) are plotted against the intensity of the corresponding voxel in image B, B(x_A). When misregistration is greater between the two images, the 2D histogram displays a more disperse or blurred distribution. When these histograms are normalized by the total number of voxels, N, the result is the joint probability distribution function $p_{A,B}^{T}$ of image A and B. The equation for joint entropy is provided below in, Figure 11.

Figure 11: Joint Entropy

$$H(A,B) = -\sum_{a}\sum_{b} p_{AB}^{T}(a,b)\log p_{AB}^{T}(a,b)$$

As medical images have many intensity values, up to 4096 for MR and CT images, the probability distribution function becomes very sparse. Binning these intensities into bins is commonly used to address this problem. The intensity values are typically binned to 32 to 256 bins. Therefore, in the equation for joint entropy, a and b can refer to the image intensities themselves or to a representative bin of image intensities.[65] Joint entropy is highly dependent on T, or the transformation. In fact, the probability distribution function of A and B, $p_{A,B}^{T}$, is highly dependent on the overlapping domain of the two images, $\Omega_{A,B}^{T}$. This presents a problem, in that a registration algorithm utilizing joint entropy will tend to maximize regions that contain noise in the lowest intensity value bins, potentially providing an incorrect solution.

2.2.2.1 Mutual Information

Mutual information provides an advantage over joint entropy by considering separately the information provided to the overlapping volume from each individual image. In other words, mutual information considers the marginal probability distributions of each image, as well as the joint information, or the joint probability distribution function. This method is represented in Figure 12.

Figure 12: Mutual Information

$$I(A,B) = H(A) + H(B) - H(A,B)$$

or

$$I(A,B) = \sum_a \sum_b p_{AB}^{\mathrm{T}}(a,b) \log \frac{p_{AB}^{\mathrm{T}}(a,b)}{p_A^{\mathrm{T}}(a) \cdot p_B^{\mathrm{T}}(b)}$$

At the best alignment between the two images, mutual information is maximized, meaning that the combined uncertainty of the two images is less than the sum of the uncertainties of the individual images. As mutual information is improved, one image becomes a good predictor of the values of the other image, meaning that knowing the value of voxel intensities of one image diminishes the uncertainty (entropy) of the corresponding voxel in the other image.

2.2.3 Optimization

In general, optimization of a registration algorithms involves selecting a cost function or similarity metric, computing this value for the current registration, and iterating the parameters of the transformations to increase or decrease this metric until the maximum or minimum result within the given boundary conditions is obtained. The iterations continue until the similarity measure converges to where no other transformation can provide a more 'optimal' measure. The number of iterations can be constrained to cease at a maximum number of iterations or at the iteration at which the difference between measured similarity between sequential iterations is below a set threshold.

Optimization can potentially end in a convergence to a local maximum or minimum of the similarity measure. To avoid this situation, providing a best starting transformation is suggested, minimizing the possibility of reaching a local optimum before reaching the end desired global optimum. However, there may be several optima

within a given parameter space. To accommodate this challenge, multi-resolution registration has become useful. By blurring an image prior to the first iterations of registration, local optima may be removed to provide a better initial transformation. As each lower resolution transformation is optimized, the resolution is increased to better fine tune the similarity of the registered images. This is known as multi-resolution registration.[65]

Non-rigid algorithms generally require additional parameters to define the transformation than rigid or affine methods, and, therefore, require more time to determine the appropriate optimizer. In addition, an optimal parameter set may provide a visibly adequate image result, but may not be anatomically or physiologically meaningful throughout the image space. Folding or tearing of the image may be present after deformation – a result that is physically invalid in medical applications. Therefore, the appropriate optimization for the given registration problem is dependent upon the similarity metric, the type of transformation used, any resource constraints employed under the implementation circumstances, and the level of precision or accuracy desired from the results, which includes the level of physical reality needed in the results. [65]

2.2.4 Cardiac Image Registration

Although there are many applications of registration algorithms in the subject of medical imaging, this work focuses on registration of cardiac images. Each imaging modality has devised imaging methods to capture changes in the motion of the heart over time, such as contrast enhanced multi-phase CT imaging, PET multi-phase perfusion images, and tagged magnetic resonance imaging.

Frangi et al. has written an extensive review on the many forms of 3D modeling of the heart for functional analysis.[72] The work summarizes several modeling methods and categorizes them into imaging modality, complexity, pre-processing, automation, and available validation. The general takeaway concludes that 3D cardiac modeling approaches do have the capability to improve diagnosis of cardiac imaging, but available studies at the time of the review still required improved robustness, computational simplicity, and clinical validation. The review also focused on functional analysis metrics that studied volumes and volume changes as opposed to dyssynchrony and mechanical dysfunction. The metrics included left ventricular volume, left ventricular mass, stroke volume, ejection fraction, and cardiac output. The study did touch on motion and deformation analysis metrics, such as wall thickening, which has demonstrated a higher sensitivity for dysfunctional contraction over wall motion[73], and strain analysis, which could be a promising method to quantify ventricular deformation.

Non-rigid registration has been extensively studied in the case of tagged magnetic resonance imaging by Chandrashekara et al., who employed 2D and 3D multi-resolution, free form deformation approach on cardiac images, utilizing normalized mutual information algorithm optimization on short-axis and long-axis images [56,63]. Motion fields were extracted from the algorithm for several systole images registered to the target diastole image. This method demonstrated a root-mean squared (rms) tracking error of less than 2 mm for most of the patient data tested, which was calculated between the in-plane displacement estimated from registration and that measured by an observer.[56,63] As the approach used in this study did not make any assumptions regarding the imaging

modality, it can theoretically be applied to any images, for example untagged MR, ultrasound or CT.

Chandrashedara et al. further supplemented this work on tagged MR images by developing a 4D B-spline transformation approach with the maximization of mutual information. In this work, the systole images were registered to a diastole image. They proposed use of these deformation results for quantification of strain and velocity analysis.[62] Supplemental studies by the group applied this algorithm to synthetic data with a known transformation. [64]

As summarized by Frangi et al.,[73] characterizing ventricular wall motion has proven to be a complex problem. The aim of these studies was to provide a repeatable tool to assess myocardial regional wall motion to address the subjectivity presented by the standard visual wall motion scoring (VWMS) methods suggested by the American Heart Association (AHA). VWMS involves segmentation of the myocardium into 17 regions, each of which are graded on a five level scale as normo-kinetic, mild-hypokinetic, severe hypokinetic, akinetic and dyskinetic. As these regions are assessed qualitatively by the clinician, the method suffers from high interobserver variability, introducing non-reproducibility and subjectivity. In the studies described by Frangi et al, an extensive number of MR images were acquired from healthy individuals to train a statistical model of normal myocardial function. The methods employed a statistical model to identify local ventricular contraction patterns from the normal examinations. In addition, this method involved the contouring of end diastole and end systole wall components, epicardium and endocardium, and unification of all normal contours to a unit contraction model using thin-plate spline warping. It was then necessary to

determine the number of independent components into which to sort the statistical model components. A clustering technique was used to segment the components. Once the components were identified, the density function of each component was determined. They then employed a means to identify wall abnormalities based on this statistical model. By comparing the component values of an abnormal individual to the distribution of the normal statistical model, a region could be flagged as deviating from the normal myocardial contraction with different degrees of deviation from the statistical model values.

Suinesiaputra et al.[74] used a statistical model based on a database of normal myocardial images to establish whether and to what degree a region was abnormally contracting. This method requires a representative normal database of cases to which to compare other suspected abnormal cases. This method appears to be viable in other areas of the heart, for potential interventricular contraction analysis or even atrial to ventricle contraction efficiency analysis.

Computed tomography images are relatively unstudied for the extraction of wall tissue motion fields within the referenced work. As these images are routinely acquired for planning of cardiac catheterization procedures, such as radiofrequency ablation and biventricular pacing, developing a registration algorithm to extract the motion fields for the myocardial tissue could contribute an additional use of images that already are routinely used for general anatomical reference. Chapters 3 and 4 will describe the implementation of a non-rigid registration algorithm for use with multi-slice multi-phase cardiac computed tomography images. Like the pre-existing work, this investigation will attempt to characterize the difference in motion fields between a normal clinical study

and one with known myocardial function pathology. Unlike the preexisting work, however, a statistical model of what constitutes ‘normal’ myocardial function has not been established. Instead, only one example of a normal motion will be used for an initial comparison to a pathological case to identify gross differences in the types of motion fields within the myocardium.

CHAPTER 3 REGISTRATION ALGORITHM DEVELOPMENT, VALIDATION AND OPTIMIZATION

3.1 Methods

3.1.1 Algorithm Overview

As described in Chapter 2, placing a pacing lead at the site of the most delayed motion has the potential to provide improved pacing results. The challenge remains of identifying the site of the most delayed region prior to lead placement. Previous work implemented registration algorithms for cardiac MR and developed statistical models for identifying regions of abnormal wall motion. While promising, MR acquisitions are not routinely prescribed prior to CRT, due partly to issues of cost. As CT imaging is often performed as part of resynchronization treatment planning and is a fast and accessible means of imaging, extending a registration method to assessing left ventricular motion of CT images could provide another means of reproducible contractility assessment. The purpose of this study is to develop and implement a 3D non-rigid registration algorithm for motion analysis of multi-phase cardiac CT images.

Figure 13 displays the overall goal of the proposed motion analysis algorithm. The first step of the analysis performs registration to determine the motion vectors of left ventricle. Analysis of the images requires registration of each phase image (source image) to a reference image (target image). When one image is registered to another image , a transformation matrix is calculated that defines the motion necessary to

transform the original source image to the new image. The transformation matrix can be used to evaluate the motion characteristics between the two images.

Figure 13: A Method for Non-rigid Registration for Motion Analysis

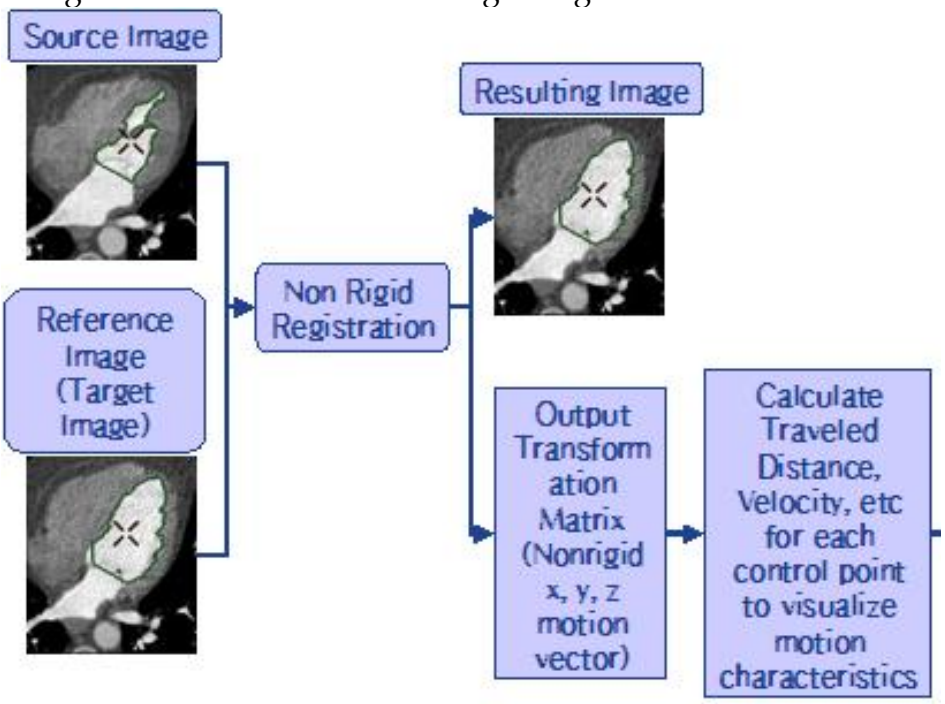

This work developed a multi-resolution non-rigid registration algorithm that used mutual information as the similarity measure and B-Splines as the transformation model. The optimization method used a brute-force search, whose extent was determined by the user-defined parameter of step length. Figure 14 summarizes the registration algorithm framework which is explained in more detail in the following paragraphs..

Figure 14: Registration Algorithm

```
calculate similarity value (MI) between images
for all resolution levels (lowest to highest)
   for  all step lengths (largest to smallest)
        initialize control points
        for  all control points (first to last)
                translate by step length (x, y, z)
                interpolate (B-Spline) to new transformed image
                calculate similarity value (MI) for new image and
                compare to previous
        end
        translate control point that maximizes similarity
    end
end
```

The iterative algorithm begins by defining a source image and a target image, and calculating the mutual information between the images. A rectangular grid of control point locations is defined in the source image. The algorithm starts with the lowest resolution level, which corresponds to a coarsely spaced grid of control points. The algorithm then translates the voxel at a selected control point in an initial direction by a distance equal to the step length. After the voxel location is adjusted, the remaining voxels are transformed non-rigidly according to B-spline interpolations. The mutual information between the target image and transformed source image is recalculated. If the transformation results in increased mutual information, the adjustment is maintained. If the transformation reduces the mutual information, the original voxel is translated by the step length in the next direction. This adjustment is repeated for each control point. Using the coarsely transformed source image as the initial guess, the process is repeated

with a smaller step length. Thus the image is first transformed on a course scale using large step lengths, and the transformed image is refined by repeating the optimization with a finer step length. This iterative process is then repeated at a higher resolution level, which is obtained by using a finer grid to define the control points. Overall, the search for the optimal transform is repeated for all control points, for all step lengths and then for all resolution levels until the number of iterations specified by the user.

Two outputs are generated by the completed algorithm: (1) the optimally transformed source image and (2) the array of transformation vectors which define the optimal motion of each control point from the target image to the source image.

3.1.2 Implementation

The registration algorithm was implemented using the VTK CISG Registration Toolkit 2.0.0 (http://www.vtk.org/pipermail/vtkusers/2002-September/062841.html) and Matlab 7.4.0 software. The VTK CISG Registration Toolkit is a free software package that provides two voxel-based, mutual information image registration algorithms and is implemented on top of the Kitware 4.0 Visualization Toolkit (VTK). It allows for registration implementations on Linux, Solaris, and Windows computer hardware and operating systems. The developed algorithm included the following user-defined parameters: the number of resolution levels, number of histogram bins used to calculate the mutual information, the number of allowed iterations, the number of resolution steps, length of resolution steps, similarity measure (options include mutual information or normalized mutual information), and control point spacing. Matlab was used for

processing of motion vectors obtained from the registration process and for creation of synthetic datasets used for validation.

3.1.3 Validation of Registration Functionality

The registration algorithm was validated using three main methods, including validation of the non-rigid algorithm on non-rigid motion of an elliptical synthetic data series, and validation of the non-rigid algorithm on clinical cardiac image data.

3.1.3.1 Validation with Prescribed Motion of an Elliptical Synthetic Data Series

For the first state of validation, a simple ellipse was developed (Synthetic Dataset A), which contained increasing voxel intensities from the center of the ellipse outward. This simplified data series is shown in Figure 15. The figure demonstrates only one slice through the center of the data ellipse. The synthetic ellipse object was defined over121x121x121 voxels with a dynamic range of 4400 intensities.

Figure 15: Synthetic Elliptical Data Series

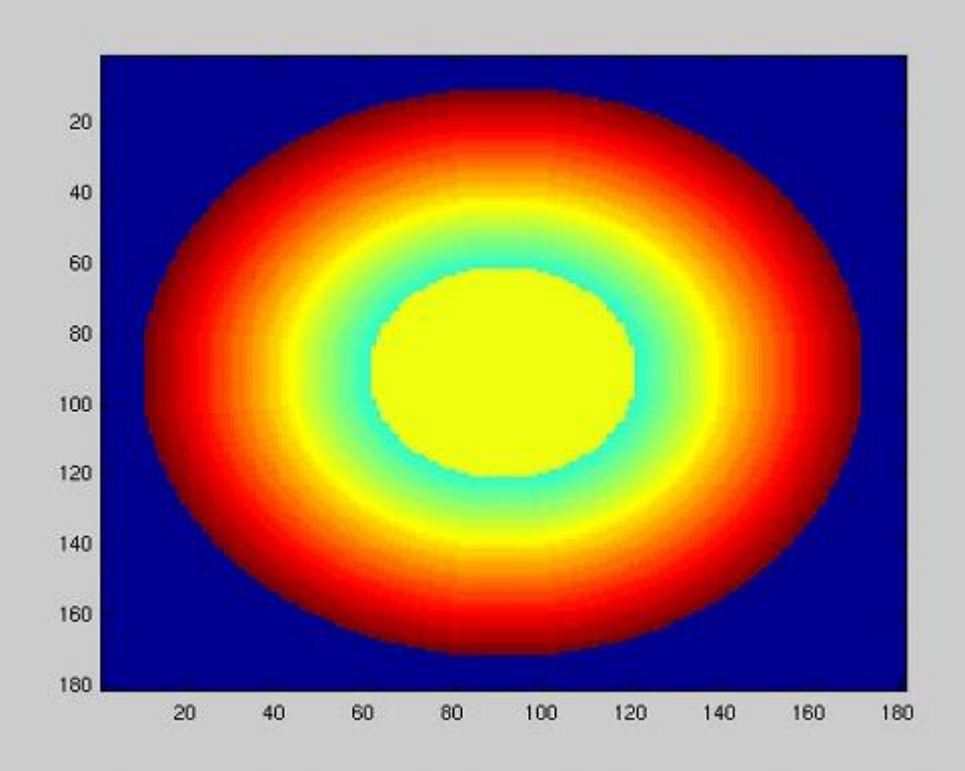

To validate basic algorithm functionality and investigate the effects of the algorithm parameters, the ellipse image (Synthetic Dataset A) was transformed non-rigidly using a prescribed transform, with each voxel moving in the direction outward from the center of the ellipse. The magnitude of motion increased as the distance between the original voxel location and ellipse center increased. Figure 16 shows an example of the prescribed vector motion at one slice location within an ellipse with a radius of six voxels.

Figure 16: Prescribed Vector Motion of Ellipse

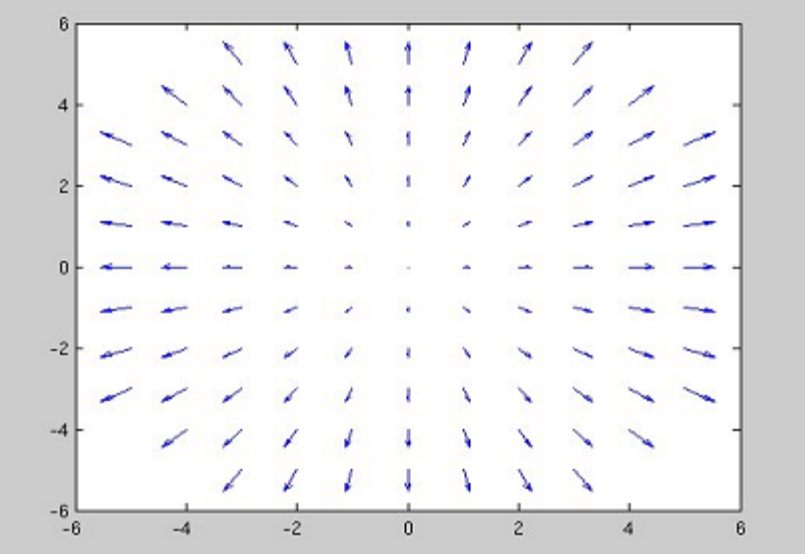

The transformed image, Synthetic Dataset B, was generated by simulating non-rigid motion of the voxels using B-spline interpolation.

Figure 17 displays the original synthetic images on the top (left to right shows the xy, or axial, plane, xz, or coronal, plane, and yz, or sagittal, plane) and displays the non-rigidly deformed images on the bottom (same orthogonal views as the original synthetic data).

Figure 17: Original Synthetic Data and Artificially Transformed Data
Original synthetic images on the top (left to right shows the xy, or axial, plane, xz, or coronal, plane, and yz, or sagittal, plane)
Non-rigidly deformed images on the bottom (left to right shows the xy, or axial, plane, xz, or coronal, plane, and yz, or sagittal, plane)

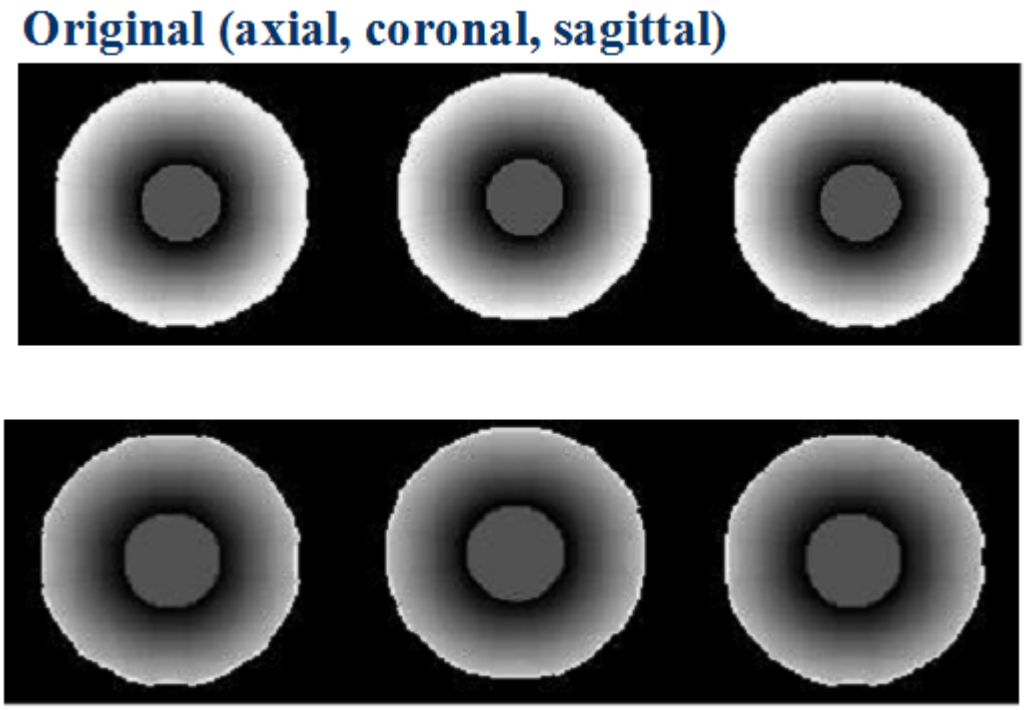

The original (Synthetic Dataset A) and transformed (Synthetic Dataset B) images were registered using the developed non-rigid registration algorithm. The estimated transformation result was then compared to the prescribed transformation to quantify the performance of the algorithm. The mean-squared error between the prescribed and estimated motion vectors was the quantitative metric used to evaluate the algorithm.

To investigate the effects of the algorithm parameters, a design of experiments (DOE) was performed while varying several of the algorithm parameters. The number of resolution levels was varied between 1, 3, and 4, as this range was found through preliminary testing to be computationally feasible with respect to memory consumption,

which will depend on the type of system being used. The number of histogram bins was varied between 32, 64, and 128, in order to investigate the tradeoff between computational complexity and high intensity resolution during the mutual information calculation. Finally, the control point spacing range was determined by running a few algorithm runs on the data to understand the range that would provide a number of degrees of freedom for which the hardware and software could proceed without aborting the registration process. Based on these preliminary runs, the control point spacing was varied between 8, 10, and 12mm. For each run of the DOE, the MSE between the prescribed and estimated motion vectors was used to quantify algorithm performance

3.1.3.2 Feasibility with Clinical Data

The registration algorithm was then tested on a normal clinical image series (Clinical Dataset X). A systole image volume was registered to a diastole image volume. The end diastole image was selected as the target image because this cardiac phase demonstrates the largest volume of the cardiac cycle. This is consistent with the work of Chandrashekara et al.,[56] which also utilized end diastole as the target image series. The transformed image series was compared qualitatively to the diastole image to understand in which regions of the ventricle the registration algorithm provided discrepancies between the target and transformed image volumes. This information was used to understand some of the limitations of the registration algorithm for use in motion analysis.

3.1.4 Optimization of Algorithm Parameters

A second design of experiments (DOE) was developed to analyze the performance of the registration algorithm. The design of experiments (DOE) was performed on the clinical data (Clinical Dataset X), using the end diastole and end systole phase images, with three levels for number of resolution levels (1, 3, 4), number of histogram bins (32, 64, 128), and control point spacing (8, 10, 12). These values were chosen for consistency with the initial synthetic data analysis. For each run of the DOE, the end systolic phase image (phase 4) was used as the source registration phase and the end diastolic phase image (phase 1) was used as the target registration phase. Figure 18 summarizes the parameters used for the design of experiments.

Figure 18: Registration Algorithm Parameters

Parameter	Description	Range
Similarity measure	Metric used to compare registered images. Maximized during registration process	MI
Interpolation model	How transformed image is calculated	B-Spline
# of histogram bins	Used to calculate similarity measure.	32, 64, 128
# of iterations	Maximum number of iterations per optimization.	100
# of steps	Number of different step sizes.	8
Length of steps	Length of the initial step size.	1
Lambda	Weighting factor for the smoothness constraint	0
Control Point Spacing	Spacing between vertices of the mesh grid. The vertices of the mesh grid are the control points.	8, 10. 12

Unlike the ellipse simulation, the true motion vectors are not known in the case of clinical data. Therefore, the mutual information between the target image and the final registered source image was compared for each combination of algorithm parameters to quantify the performance of the registration. The registration parameters that yielded the

greatest mutual information were chosen as the optimal parameters and used in the study of clinical motion analysis described in Chapter 3.

3.2 Results

3.2.1 Validation of Registration Functionality

3.2.1.1 Validation with Prescribed Motion of an Elliptical Synthetic Data Series

The transformed ellipse dataset (Synthetic Dataset B) underwent several registrations in which the number of resolution levels, number of histogram bins, and control point spacing was adjusted within a formal design of experiments. Below, Figure 19 displays the original series (Synthetic Dataset A - top), the artificially transformed image series, (Synthetic Dataset B – middle), and the resulting registered image series (Synthetic Dataset C - bottom) after registration.

Figure 19: Synthetic Data Before and After Registration
Original diastole image on top (Synthetic Dataset A), artificially transformed image in middle (Synthetic Dataset B), and the non-rigidly registered image on bottom (Synthetic Dataset C)

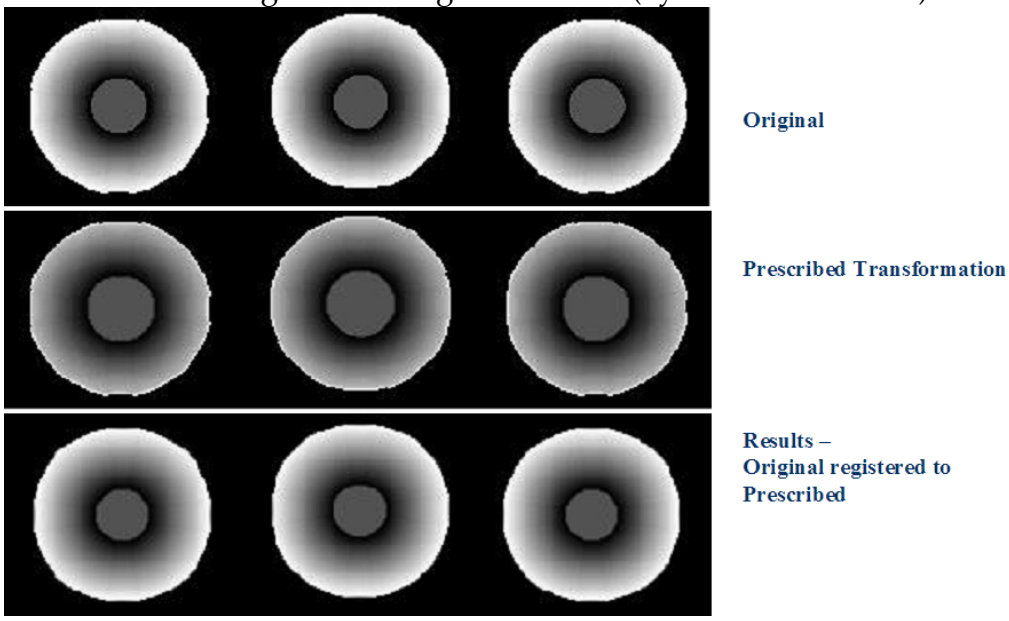

Figure 19 displays the original diastole image (top), the image with the prescribed transformation (middle), and the non-rigidly registered image overlaid on top (bottom). From left to right, the figure displays the axial, coronal and sagittal views of the image series. These images show that there is a good overlap between the original series and the registered series. The purpose of the registration was to transform the synthetically transformed series into the original series. The inner radii of the ellipsoids are not fully registered, but the other portions of the ellipsoids demonstrate reasonable agreement.

The compiled results from the design of experiments are present in Figure 20. The average root-mean squared error between the prescribed motion vectors and the vectors estimated by the registration algorithm was calculated for each run of the DOE.

The minimal root-mean squared error is highlighted in the figure, as 0.0587. This minimal value was obtained using three resolution levels, 128 histogram bins, and a 12-mm control point spacing. As the maximum motion introduced into the image series was approximately 7.5 mm, an RMS of 0.0587 demonstrates an error of less than one percent of the maximum motion imposed on the ellipse, implying a good result. As validation of a registration algorithm for use in medical imaging relies on the clinical impact as well as the quantitative values that one can extract, it would be important to also consider the time to image, or the time it takes to get to the resulting registered image, and the realistic anatomical nature of the resulting registered image. Most of the RMS results are clustered from about 0.06 and 0.1 mm. If one reviews the interactions between the DOE factors – resolution levels, histogram bins, and control point spacing – one can recognize which of these factors has the largest effect on the resulting RMS. The DOE interactions

plot in Figure 21 demonstrates that the control point spacing has the highest effect on the RMS registration result.

Figure 20: Non-rigidly Transformed Ellipse Design of Experiments Results

No of res levels	No of histo bins	Control Point Spacing	Avg_RootMeanSquaredError
1	128	10	0.0843
4	64	8	0.1036
1	128	12	0.0643
4	64	10	0.0784
1	32	8	0.1108
3	128	10	0.0799
4	128	12	0.0603
4	64	12	0.0619
3	128	8	0.1072
3	64	12	0.062
3	32	10	0.0834
4	32	12	0.0645
1	64	8	0.1104
3	64	8	0.1077
1	64	10	0.0838
1	128	8	0.1105
4	128	8	0.1082
3	32	8	0.1108
4	128	10	0.08
1	64	12	0.0639
4	32	10	0.0837
3	128	12	0.0587
4	32	8	0.1096
3	32	12	0.0645
1	32	10	0.0845
1	32	12	0.0646
3	64	10	0.0818

Figure 21: DOE Factors Interactions
Demonstrates the interactions between the DOE factors and the resulting RMS values

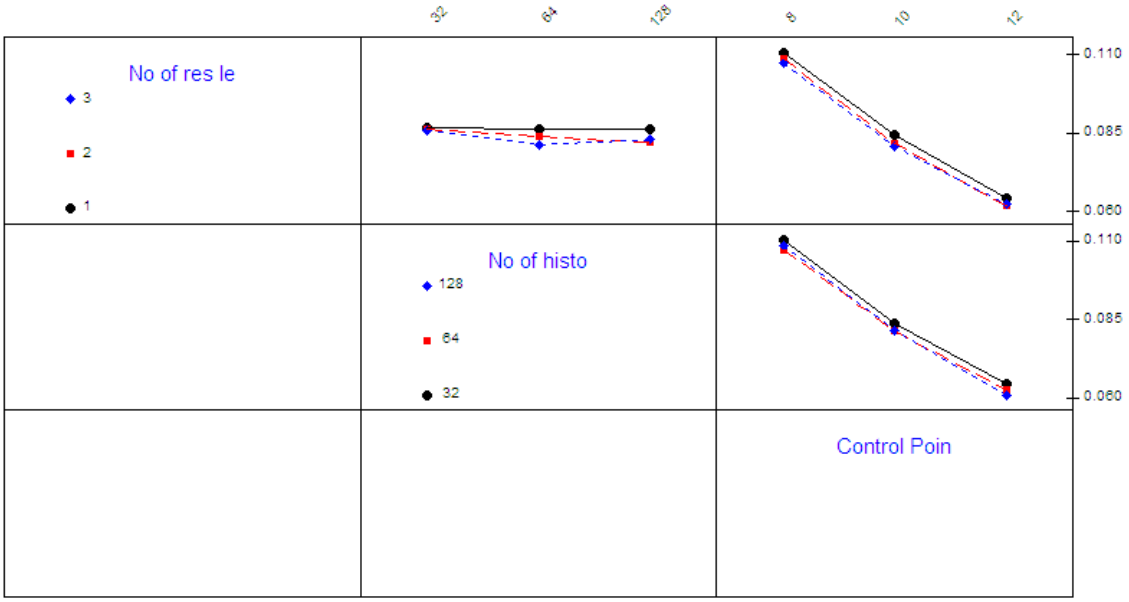

If one considers the processing time required for more resolution levels and the use of more histogram bins, one might consider using the most time-efficient parameterization for those factors rather than that of the resulting 'optimal' RMS. In this specific example, using one resolution level and 32 histogram bins would have minimized the processing time required for the analysis of those parameters. In the clinical setting, however, one would also need to consider if and how significantly the results changed clinical treatment. If, for example, using the most time efficient number of resolution levels and histogram bins, 1 and 32, respectively, had an undesired clinical outcome, the operator would have to consider using the necessary parameters to obtain the proper clinical outcome.

3.2.1.2 Feasibility with Clinical Data

Once the synthetic data was reviewed, the registration was applied to a clinical data series (Clinical Dataset X). As already stated, the systolic phase of the series (phase 4 of 10) was registered to match the diastolic phase of the series (phase 1 of 10). Figure 22 displays a visual representation of the original phases, systole (left) and diastole (middle), and the non-rigidly deformed systolic phase, Clinical Dataset Y (right).

Figure 22: Registration of Systole to Diastole Phase
(Left) Systole Phase, (Middle), Diastole Phase, (Right) Systole Phase Registered to the Diastole Phase
(Top) Axial Planes, (Bottom) Coronal Planes

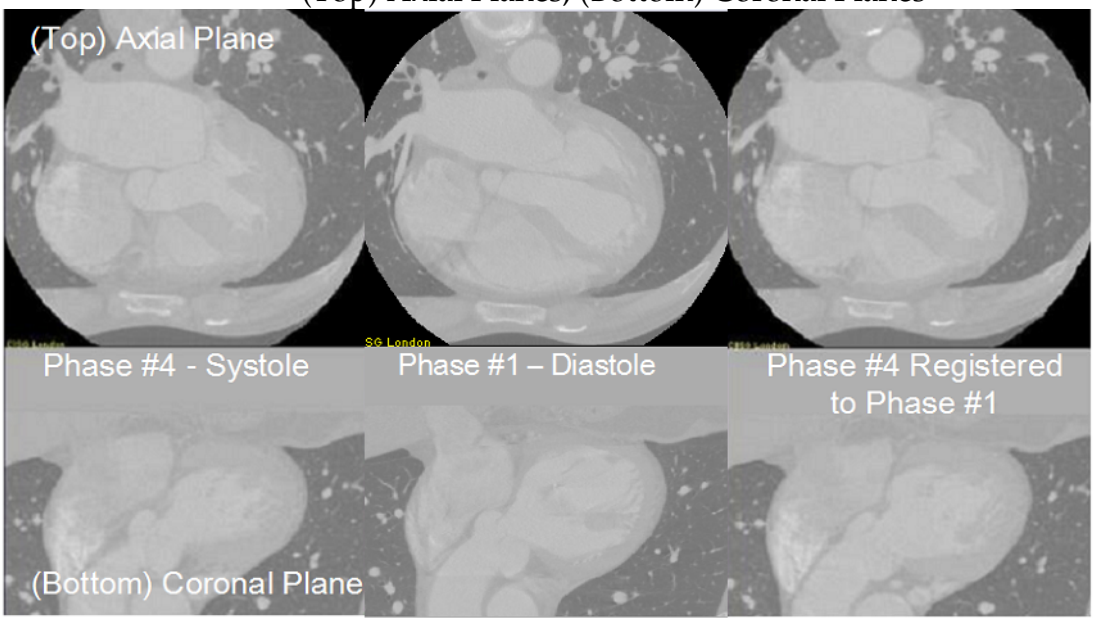

As the purpose of transforming the systole image was to register it to the diastole image, the diastole image and transformed systole image were overlaid to view where the registration succeeded in the transformation and where differences could be observed. A difference image was created from the diastole (Clinical Dataset X) and transformed systole images (Clinical Dataset Y) by subtracting the two images. Figure 23 shows the original diastole image (grayscale) with the difference image overlaid on top (hot iron

color overlay). The areas of yellow highlight the regions in which the highest difference was noted.

Figure 23 Diastole of Clinical Dataset X and Clinical Dataset Y Difference Overlay

Original diastole image (grayscale) with a difference image (created from a difference of the diastole and registered image) overlaid on top (hot iron color overlay)

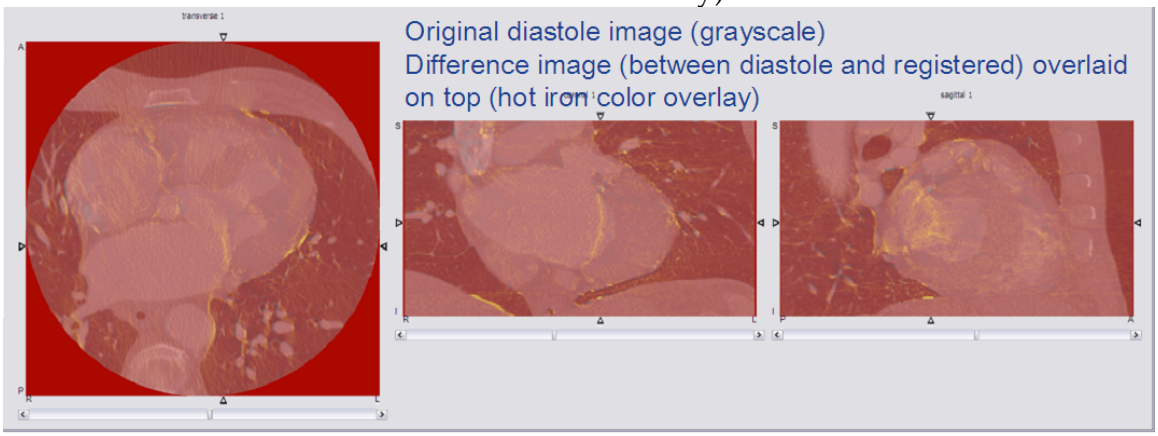

The regions of highest difference appear to occur at the mitral value, the coronary vessels, and the pericardial sac. With regard to the mitral valve and coronary arteries, these areas are likely to have discrepancies based on contrast enhancement differences occurring between the original images. As the heart pumps, the contrast flows through these regions, causing intensity differences that will be picked up on this difference image. With regard to all of these regions, higher motion of these regions – opening and closing of the valve, pulsatory motion of the arteries, and breathing effects on the pericardial sac – is likely to cause some differences between the diastole and transformed systole images. In general, differences in other areas of the image were minimal, suggesting reasonable registration of the systole image to the diastole image.

3.2.2 Optimization of Algorithm Parameters

3.2.2.1 Design of Experiments

Figure 24 displays the results from all runs of the design of experiments. The left-most column lists the mutual information of the transformed source image and the target image.

The maximum mutual information of 1.391 was obtained using the algorithm parameters of one resolution level, 64 histogram bins, and a control point spacing of 8-mm. Various runs of the DOE results could not be completed due to the memory limitations of the algorithm and system used for registration. These runs, marked as ‘na’, failed to complete registration and aborted before final registration could be obtained. In general, these failed runs involved multiple resolution levels. Due to the length and analysis requirements for these problematic runs, these parameterizations would likely be less clinically desirable for the analysis time and resource constraints.

A maximized MI of 1.391 is only one quantitative approach to optimizing the registration for these clinical image series. If one considers that the MI value of the diastole image when registered with itself is approximately 2.65, one might consider this value the upper limit of how maximized the MI could be in an ideal registration scenario.

Figure 24: Design of Experiments Results

RunOrder	Number of resolution levels	Number of histogram bins	Control Point Spacing	Mutual Information
1	1	128	10	1.361
2	4	64	8	na
3	1	128	12	1.361
4	4	64	10	1.376
5	1	32	8	na
6	3	128	10	na
7	4	128	12	na
8	4	64	12	1.362
9	3	128	8	na
10	3	64	12	1.367
11	3	32	10	1.379
12	4	32	12	1.362
13	1	64	8	1.391
14	3	64	8	na
15	1	64	10	1.342
16	1	128	8	1.345
17	4	128	8	na
18	3	32	8	na
19	4	128	10	1.381
20	1	64	12	na
21	4	32	10	na
22	3	128	12	1.367
23	4	32	8	na
24	3	32	12	1.364
25	1	32	10	1.159
26	1	32	12	1.313
27	3	64	10	1.382

As many of the DOE runs result in values differing only by a few hundredths of a unit, one must additionally consider other factors that differentiate the results. This quantitative value, as stated before, does not represent the clinical usefulness or efficacy of the resulting registration. To further validate these results, other tests could be performed. One example of this might include comparing the resulting motion transformations from the registration algorithm to an operator defined motion

transformation, wherein a clinical expert could identify landmarks in the systole image and the location of these same landmarks in the diastole image. Comparing the calculated motion between the operator defined landmarks and the motion transformation calculated for the respective control points of the source image could provide a means to compare the motion transformation value to a ground truth motion value as determined by an operator. An alternative validation approach, which would be far more invasive and more appropriate for an animal study, would be to place radio opaque fiducial markers on the epicardium to act as landmarks that could be easily identified on images. The subject could be imaged and motion of the fiducials could be compared to the motion of the nearest neighboring control points.

3.2.2.2 Conclusion

A method of non-rigid 3D registration was attempted between a systolic and diastolic cardiac image utilizing mutual information optimization and B-Spline transformation. Reasonable registration between the target and source clinical images were obtained, providing an x, y, and z coordinate that described the motion of each control point to describe the transformation. The maximum mutual information of 1.391 was obtained using the algorithm parameters of one resolution level, 64 histogram bins, and a control point spacing of 8-mm.

CHAPTER 4 MOTION ANALYSIS

4.1 Methodology

The results of Chapter 2 indicate that the developed non-rigid registration algorithm can register cardiac CT images from different phases of the cardiac cycle. The ultimate goal of this project is to use the motion vectors derived from the registration algorithm to evaluate the left-ventricular wall motion throughout the cardiac cycle. As described in Chapter 1, determining regions of abnormal and delayed wall motion requires complex statistical models that are trained on numerous normal datasets. The development of such statistical methods is outside the scope of the present thesis, however, the preliminary feasibility of using the non-rigid registration algorithm to analyze the left-ventricular wall motion was evaluated by applying the algorithm to a normal and diseased clinical case. This chapter describes this preliminary analysis of the left-ventricular wall motion.

4.1.1 Clinical Datasets

Two previously acquired high-resolution multi-phase, contrast-enhanced CT image series acquired using GE (16-slice and 64-slice) CT scanners were obtained from sites that provided the clinical data to GE for demonstration and visualization purposes. IRB approval was obtained to use the previously acquired data in the current study. Two image sets were selected, one assessed as a patient with normal left ventricular wall

motion (Clinical Dataset X) and one evaluated as a pathological case, containing a ventricular dyssynchrony involving a septal delay in relation to the other portions of the left ventricle (Clinical Dataset Z). The normal dataset contained an image series subdivided into 10 cardiac phases, whereas the pathological case contained an image series subdivided into 20 cardiac phases. The pathological case was analyzed after subsampling to the phases of the normal dataset and with all available phases.

Clinical assessment was performed by Prachi Agarwal, MD of the Department of Radiology at eh University of Michigan on the pathological case to understand underlying pathology. Functional analysis revealed diffuse global hypokinesis. Additionally, there was more pronounced regional hypokinesis and myocardial thinning in the anterior, anteroseptal, inferoseptal, apical, and inferolateral segments. Left ventricular ejection fraction was calculated at 32%, supporting an inefficiency in the overall function of the heart in this case. Patient also had confirmed dilated cardiomyopathy.

4.1.2 Registration Details

The parameterization found to provide the maximum mutual information value during the DOE was used for the registration; this included 1 resolution level, 64 histogram bins, 100 iterations, 8 resolution steps, 1 mm resolution step, mutual information similarity measure, and 8 mm control point spacing. Once the registration algorithm parameters had been determined, each of the CT multi-phase clinical image series was registered to the diastole phase using the predetermined algorithm.

The multi-phase images series were divided into 10 or 20 phases of the cardiac cycle, dividing the cardiac phase into equally spaced time points. The diastole phase was determined by qualitatively assessing which phase image provided the largest volume of the left ventricle. This diastole phase was used as the reference, or target, phase of the registration. The images at every other phase were registered back to the reference diastole image. Therefore, the registration algorithm determined a motion vector for each control point between each source image series to the reference image series for each phase of the cardiac cycle.

4.1.3 Motion Extraction and Analysis

For each control point within the defined registration mesh, an x, y, and z motion component was generated by the algorithm. As this study is focused on the motion of the left ventricle, only the control points that resided on the ventricle wall or perimeter were manually segmented from the images and used for subsequent analysis, control points residing outside the left ventricle muscle or within the left ventricle blood pool were ignored.

This subset of ventricle control points was manually determined in the diastolic phase image, as this is the reference image in the registration algorithm. The control points were overlaid with the diastole image and each control point lying on the ventricle region was visually determined and recorded within a file. These control point indices were referenced when plotting or analyzing the motion values.

The wall motion occurs in three dimensions, making comparative motion assessment difficult. For this preliminary feasibility analysis, the resultant motion magnitudes were calculated at each control point. For each control point, the relative motion between each phase and the diastolic phase was plotted for each time point. The absolute motion at each phase was also plotted at each time point. This absolute motion value was calculated by subtracting the relative motion of the previous time point, which is the transformation calculated by the registration transformation, from the relative motion of the current time point. This allowed all of the phase motion values to be normalized essentially to an absolute origin of motion, which happened to be the first phase for each clinical data series. The average motion of all of the control points was also calculated. Each control point motion curve was then compared to the average motion curve to determine similarity or dissimilarity to the overall ventricular motion.

For the purposes display, the motion values are both normalized and interpolated. Normalization is performed to the sum of the motion curve to regularize the motion curve values with a consistent value. Interpolation between the discreet data points at each phase is used to create a more realistic motion curve that demonstrates a more continuous motion between the available phases. Three values are interpolated between each of the available values.

4.2 Results of Motion Extraction and Analysis

From the x, y, and z motion components available for each control point, a resultant vector was determined. The magnitude of this vector was plotted both (1) in relation to the motion of the diastolic volume, for the relative motion, and (2) in relation to the absolute motion of the point, where the previous phase motion component was removed from that of each subsequent phase, as described in the previous section. Figure 25 and Figure 26 display the relative and absolute motion curves, respectively, for the normal clinical image series, and Figure 27 and Figure 28 display the same for the pathological clinical image series. These plots include all available phases. As mentioned before, the pathological case was sub-sampled in phase to more appropriately compare to the normal image case; Figure 29 and Figure 30 display the resulting curves from that sub-sampled analysis. For each plot, the motion curve for each control point is displayed in blue and the overall mean motion curve is displayed in red.

Figure 25: Normal Relative Motion Curve

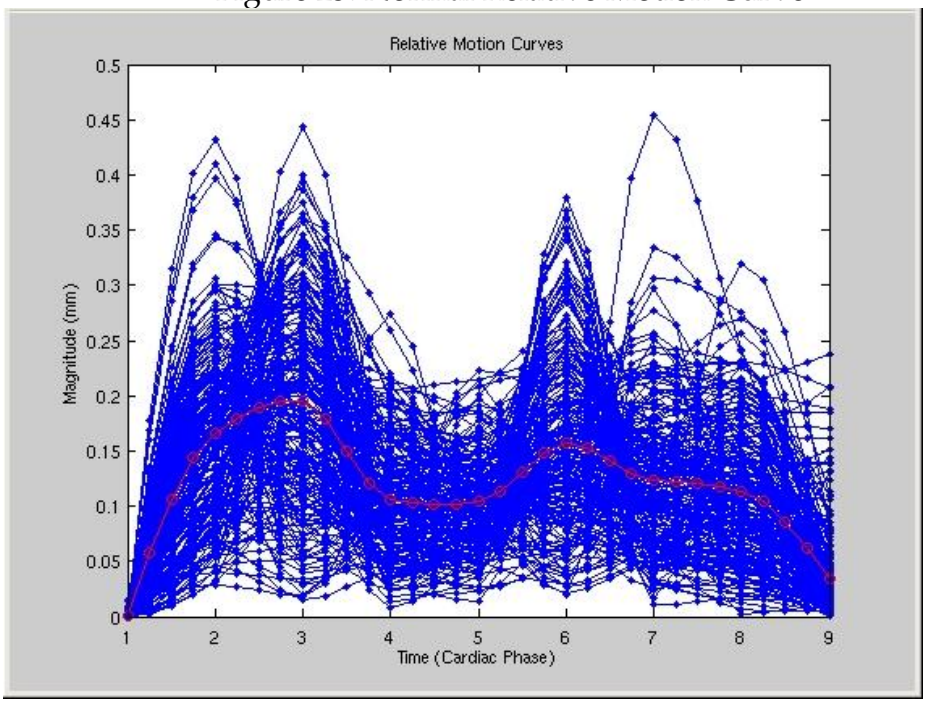

Figure 26: Normal Absolute Motion Curve

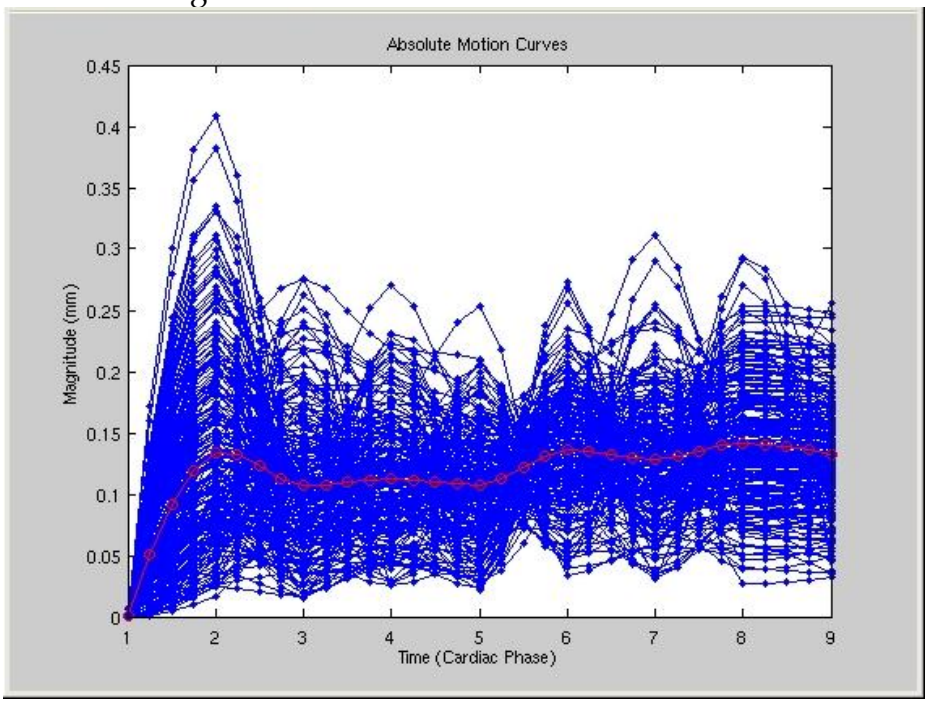

Figure 27: Pathological Relative Motion Curve

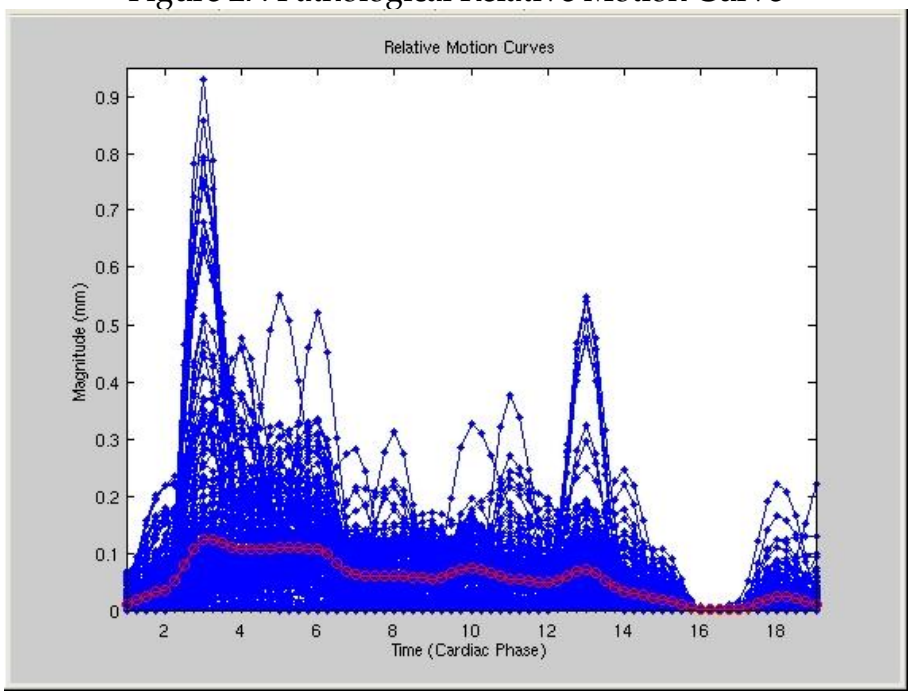

Figure 28: Pathological Absolute Motion Curves

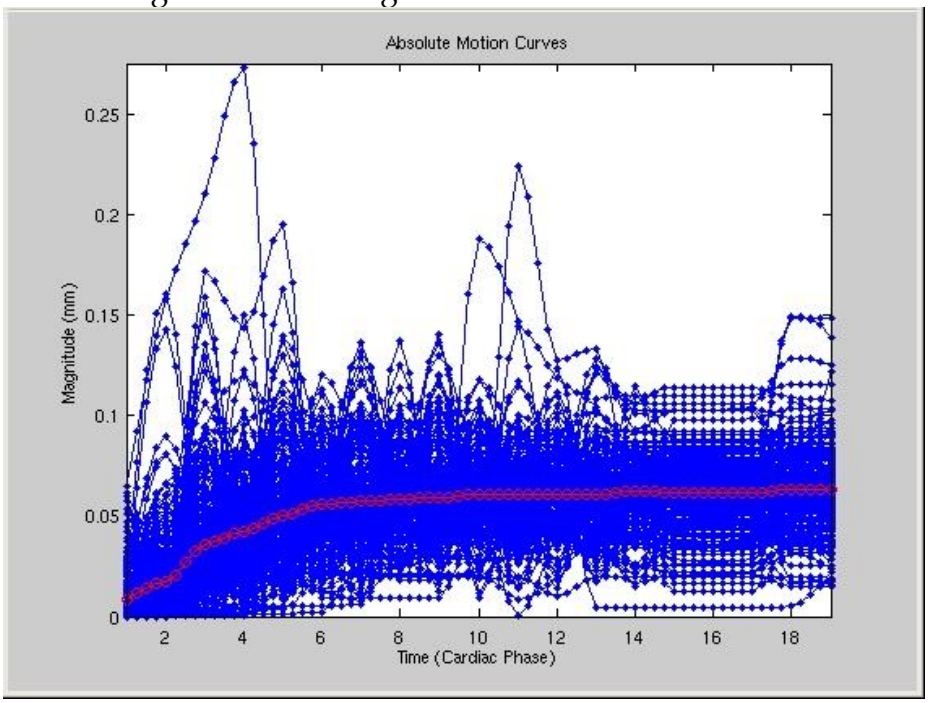

Figure 29: Pathological Relative Motion Curve for a Subset of Phases

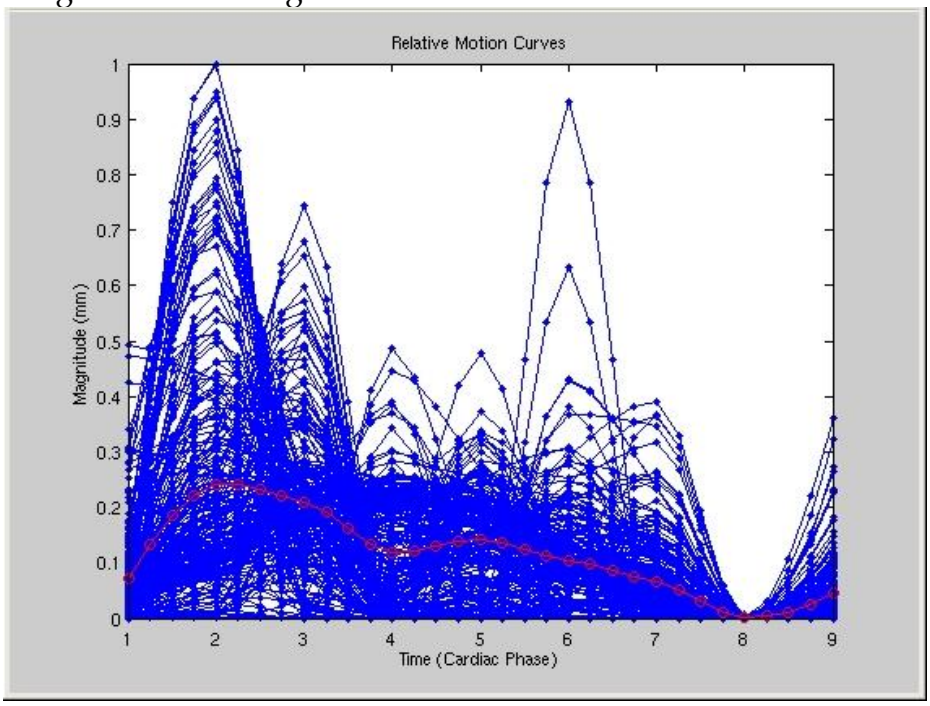

Figure 30: Pathological Absolute Motion Curve for a Subset of Phases

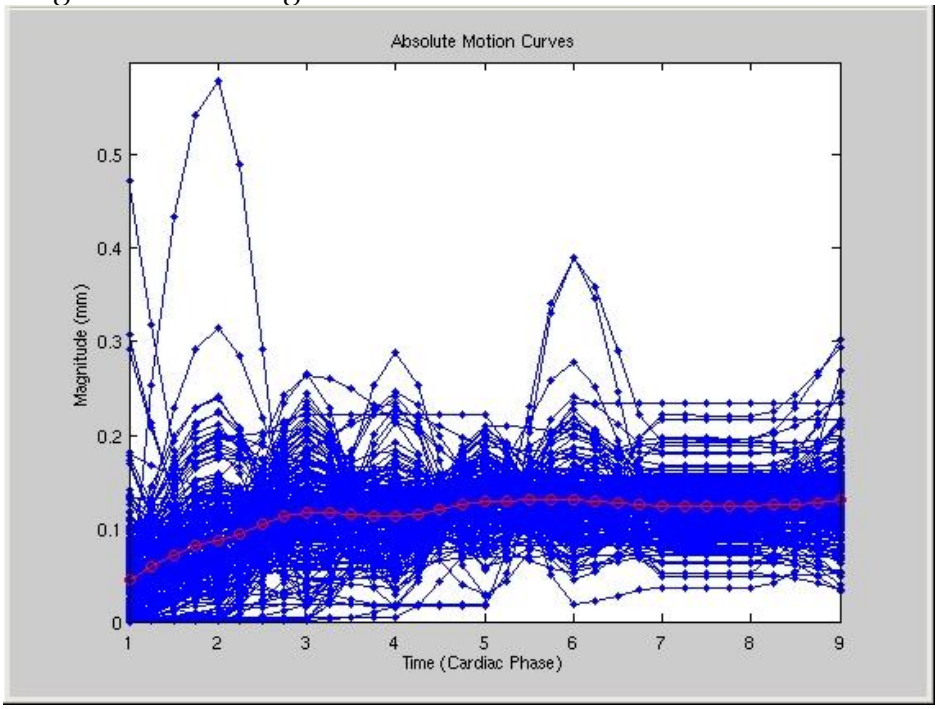

Example code for the calculation of relative and absolute motion can be found in Appendix A.

Both the relative and absolute motion curves contain differing characteristics between the normal and pathological cases. With regard to the relative motion, the normal case appears to demonstrate a bimodal motion at which there is an upswing of motion in the early phases of the cardiac cycle and another in the second half of the cardiac cycle. The pathological case appears to demonstrate a similar early phase upswing, but the latter local maxima appears more quickly and contains a smaller fraction of the first motion maxima. When comparing the normal and pathological cases with ten phases each, the absolute motion for the pathological case demonstrates fewer fluctuations within the motion. In a majority of the absolute motion curves, the pathological case demonstrates no change in the motion magnitude, whereas the normal case shows some fluctuations and a far more dynamic initial phase motion change.

Within one location of phase 8 of the pathological relative motion curve, Figure 29, the magnitude reaches a minimum where there appears to be no motion within the given phase. The absolute curve, Figure 30 between phases 7 and 8, for this same region demonstrates several ventricle control points of no change in motion. This might indicate an inefficient component of the cardiac cycle in which the heart muscle is working neither to fill or contract.

A difference in the dynamic range of the 10 phases versus 20 phases motion analysis of the pathological case can also be noted. This is due mainly to the removal of certain data points and the resulting normalization and interpolation differences that result. As experimental values are removed from the curve, the interpolation between the remaining values change accordingly. The normalization of the curve also changes because the normalization factor, or the sum of the motion curve, also changes as the inputs into the factor change.

This type of analysis makes it difficult to differentiate the motion between control points or between ventricle regions. Each motion curve is very specific to the point it represents. Certain regions of the cardiac cycle are expected to move a far less magnitude than others. Within this investigation, the motion curves could be segmented into different z-slice locations. For each of the control points, the motion curves were plotted with a different color corresponding to the z-slice location. This provides a better means of comparing cardiac regions (by z-location only) between the normal and abnormal case. Figure 31 and Figure 32 demonstrate these motion curves for the normal and abnormal cases, respectively.

Figure 31: Normal Motion Curves Segmented by Z-Slice Location
This image demonstrates the motion curves of the normal cardiac case with different curve colors per different z-slice location. The most superior z-location is displayed with darkest blue and colors progress to red as the z-location progresses more inferiorly.

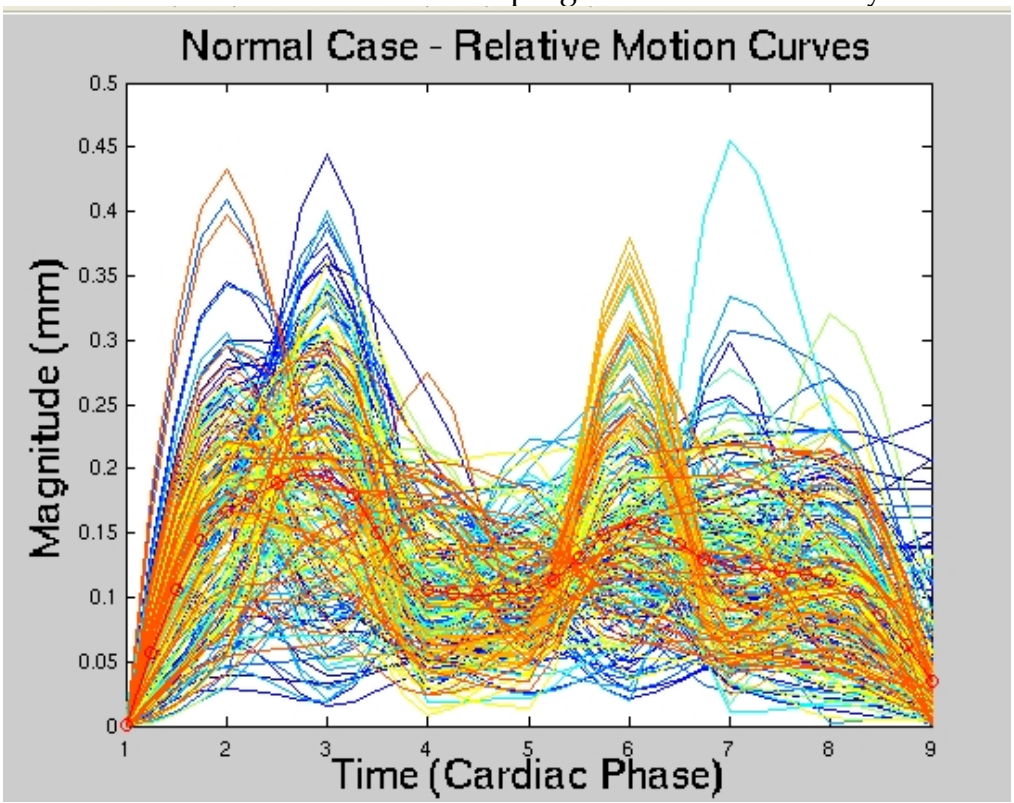

Figure 32: Abnormal Motion Curves Segmented by Z-Slice Location
This image demonstrates the motion curves of the abnormal cardiac case with different curve colors per different z-slice location. The most superior z-location is displayed with darkest blue and colors progress to red as the z-location progresses more inferiorly.

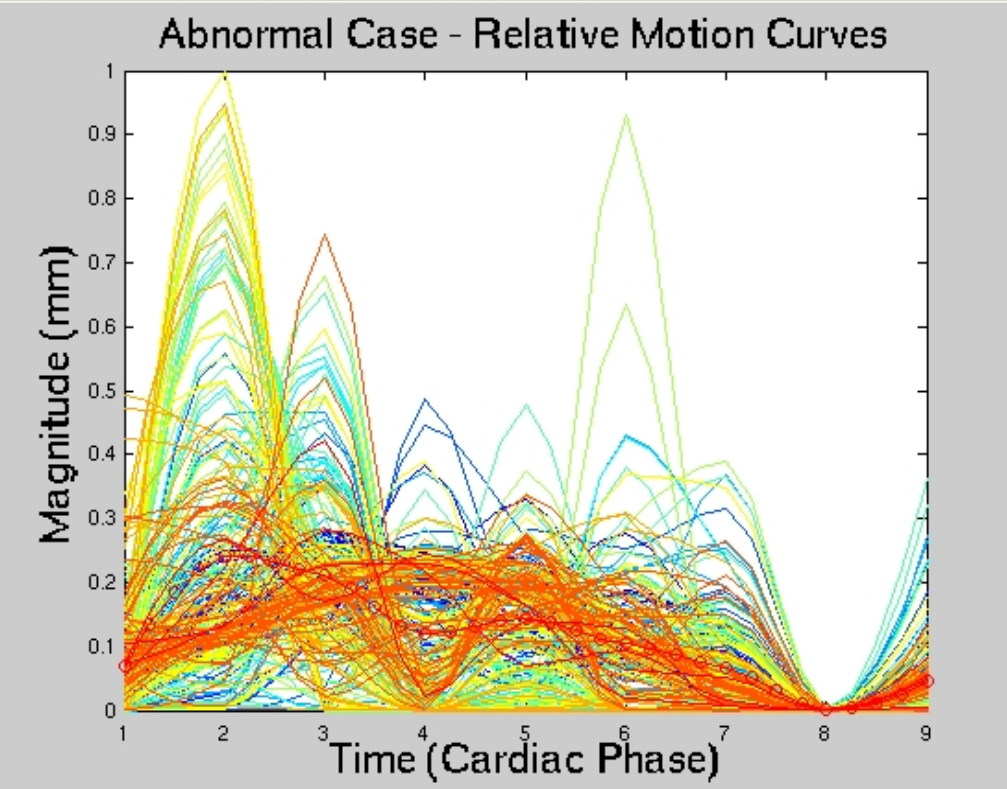

Comparing the colors between the two figures allows one to note that the comparable regions, or z-locations, between the two cases demonstrate very different motion characteristics. One can conclude from these figures that the most superior z-locations contribute more significant motion to the beginning of the cardiac motion (dark blue/cyan) in the normal case than in the abnormal case, which shows the more inferior z-locations contributing to the initial motion (yellow/orange motion curves). This type of analysis further helps to clarify the differences between the motion of the normal and abnormal myocardium. This analysis uses on the z-slice location for comparison, however. As the two cases are not from the same patient or from the same frame of

reference, the z-location does not have an exact correlation for the normal to the abnormal case, although it does have some correlation to the location of the ventricular myocardium. Compartmentalization of each control point into a standard cardiac region may make the analysis more conclusive. Using septal, lateral, basal, apical, inferior, and anterior region segmentation may make the local region comparison such that a dyssynchrony between regions can be detected. Since each of these regions moves in very different directions, it makes a resultant/magnitude analysis somewhat incomplete.

4.3 Conclusions

Overall, this preliminary feasibility investigation demonstrates that the motion vectors of a transformation between one phase of the cardiac cycle to another phase can be extracted and analyzed. This shows that the regional motion of the ventricle wall can be determined throughout the cardiac cycle using a non-rigid registration, employing mutual information optimization and B-spline transformation, and this motion can be plotted against time to visualize the changes in motion over the course of the cardiac cycle. The comparison of the motion curves, Figure 25 and Figure 29, indicates some differences between the normal and pathological cases, which may be used in future studies to identify the regions of abnormal wall motion.

CHAPTER 5 FUTURE DIRECTIONS AND CONCLUSION

5.1 Summary

This work developed a method utilizing a non-rigid registration algorithm to estimate the motion of a mesh of control points on multi-phase cardiac CT images. The algorithm parameters were optimized through a series of synthetic and clinical data experiments. After optimization, the parameters were applied to a normal and pathological clinical patient series. The motion was determined for each phase of the cardiac cycle in relation to the end-diastole image of the cardiac cycle for both series. The absolute and relative motion of each phase was extracted, demonstrating qualitative differences between the normal and pathological cases.

5.2 Registration

Where this analysis enlisted transformation between two images using a mesh of equally spaced control points, an alternative method of registration involves segmentation of the left ventricle and registration of a left ventricle surface or volume between phase images. This type of analysis would allow for other functional analysis, such as volume, mass, or cardiac output metrics, in addition to motion deformation metrics, which were the focus of this study. Segmentation of the ventricular surfaces may also facilitate analysis of wall thickening, which has proven to provide improved sensitivity over other motion deformation parameters.[73]

5.3 Motion Analysis

In this analysis, the magnitudes of the motion vectors were plotted against time for all control points or for a region or group of control points of interest. Analyzing the motion data, for example by calculating the correlation coefficient, second derivative, or Hilbert transform, the motion for each or a subset of the control points may have provided a means to identify dyssychronous motion among the ventricular points. In these methods, however, the analysis is confined to the data of the individual exam itself. A better approach may be to compare the motion analysis to a statistical model, one established from a series of images known to have normal myocardial function, similar to the previously proposed method for MR images.[74]

The motion analysis was also done on a point-by-point basis. Averages were taken from all points on the myocardial wall. Compartmentalizing the analysis into the standard 17 cardiac segments and performing an analysis on a segment-by-segment and inter-segment basis may have provided more clinically relevant analysis. Attempting to analyze each control point motion versus the average motion of all control points did not provide definitive results, mainly because the average motion curves included motion of all points, which intrinsically have different motions and may or may not have abnormal motion characteristics. This type of analysis is also complicated in that the resultant magnitude was used for motion analysis. As motion occurs in different directions for different segments, the x, y, z and angular components may be different for the motion of each segment or even each control point further complicating an attempt to compare between all points or to a mean motion curve that incorporates all points.

5.4 Conclusions

A non-rigid registration algorithm was successfully applied to multi-phase CT images, and the parameters of the algorithm were optimized through a DOE. Although the current analysis of the motion vectors may be suitable for characterizing normal versus pathological motion, the motion vector data obtained from the registration algorithm could be used in future work to determine locations of dyssynchronous ventricular motion. In addition to the potential improvements outlined already, the current study also included only one normal and one pathological case – a more diverse group of studies could have provided a better statistical analysis.

Although further investigation is necessary to assess the proposed motion analysis method, this work presents an implemented and optimized non-rigid registration algorithm. The registration algorithm was successful for extracting x, y, and z motion vectors throughout a cardiac CT multi-phase image series. Additional investigation is required to develop methods for using these motion vectors to identify the most delayed region. Visual assessment has demonstrated a difference in the motion between normal and pathologically dysfunctional image series.

A more quantitative means of analysis is desired to improve the objectivity of current motion dysfunction, however, this investigation has established a basis for doing so. This investigation demonstrated a means to characterize the normal motion of the left ventricle and comparison against the motion of a known pathological case. Future work could entail the use of a larger population of normal cases for establishing a mean and standard deviation of motion fields of normal ventricle motion. It could also entail the

analysis of numerous pathological cases, providing a characteristic motion field spectrum for each case. These pathological motion fields could then be compartmentalized into categories of similar pathological cases, differentiating pathology based on motion field spectrum.

Whereas the hypothesis for this thesis was focused on specifically finding the most delayed region of motion of the left ventricle, the potential uses for the motion fields calculated using the registration algorithm are numerous. For example, one could consider applying the same registration algorithm to any or all chambers of the heart, not just the left ventricle. Just as understanding the motion characteristics over time within the left ventricle for biventricular pacing, understanding the right and left atrial motion fields could be useful in radiofrequency ablation planning. Another example of the potential use of this type of motion characterization is stratification of different pathologies of electromechanical delay. By analyzing cardiac images of persons of different electromechanical pathology, a database of characteristic motion fields could be established. From establishing this database in conjunction with knowledge of the efficacy of different electrophysiological or pharmacological therapies, it could be possible to accumulate a database from which one could determine the best treatment to suggest for a given mechanical characterization.

BIBLIOGRAPHY

1. PW Armstrong and GW Moe. Medical advances in the treatment of congestive heart failure. Circulation 1993;88;2941-2952.

2. MR Cowie, et al. The epidemiology of heart failure. European Heart Journal (1997) 18, 208-225.

3. HJ Shenkman, et al. Congestive Heart Failure and QRS Duration: Establishing Prognosis Study. Chest 2002;122;528-534.

4. J Narula, CW Yancy, and JB Young. Preface: Primary Prevention of Heart Failure. Med Clin N Am 88 (2004) xv-xvii.

5. K Srinath Reddy and S Yusuf. Emerging Epidemic of Cardiovascular Disease in Developing Countries. Circulation 1998;97;596-601.

6. DP Zipes and HJJ Wellens. Sudden Cardiac Death. Circulation 1998;98;2334-2351.

7. Task Force for the Diagnosis and Treatment of Chronic Heart Failure, European Society of Cardiology: WJ Remme and K Swedberg. Guidelines for the diagnosis and treatment of chronic heart failure. European Heart Journal (2001) 22, 1527–1560.

8. JGF Cleland and F Habib. Assessment and diagnosis of heart failure. Journal of Internal Medicine 1996; 239: 317±325.

9. GF Tomaselli and DP Zipes. What Causes Sudden Death in Heart Failure? Circ. Res. 2004;95;754-763.

10. Heart Disease and Stroke Statistics — 2005 Update, American Heart Association. ©2005, American Heart Association.

11. CM Yu, JJ Bax, M Monaghan and P Nihoyannopoulos. Echocardiographic evaluation of cardiac dyssynchrony for predicting a favourable response to cardiac resynchronisation therapy. Heart 2004;90;17-22.

12. LA Saxon and T De Marco. Cardiac Resynchronization: A Cornerstone in the Foundation of Device Therapy for Heart Failure*. Vol. 38, No. 7, 2001.

13. D. Farwell, NR Patel, A Hall, S Ralph and AN Sulke. How many people with heart failure are appropriate for biventricular resynchronization? European Heart Journal (2000) 21, 1246–1250.

14. M Quintana, et al. Electromechanical Coupling, Uncoupling, and Ventricular Function in Patients with bundle Branch Block: A Tissue-Doppler Echocardiographic Study. Echocardiography 21: 8; 2004, 687-698.

15. JJ McMurray and S Stewart. HEART FAILURE: Epidemiology, aetiology, and prognosis of heart failure. Heart 2000;83;596-602.

16. JI Haft, MV Herman and R Gorlin. Left Bundle Branch Block: Etiologic, Hemodynamic, and Ventriculographic Considerations. Circulation 1971;43;279-287.

17. J Sorensen. PET in Heart Failure – Methods and Applications. Comprehensive Summaries of Uppsala Dissertations from the Faculty of Medicine ISSN0282-7476, http://urn.kb.se/resolve?urn=urn:nbn:se:uu:diva-4654, 2004.

18. M Breeuwer, P Johnson and M Kouwenhoven. Analysis of volumetric cardiac CT and MR image data. MedicaMundi 2003:47(2); 41-53.

19. MA Garcıa-Fernandez, et al. Regional diastolic function in ischaemic heart disease using pulsed wave Doppler tissue imaging. European Heart Journal (1999) 20, 496–505.

20. Y Koyama,T Mochizuki and J Higaki. Computed Tomography Assessment of Myocardial Perfusion, Viability, and Function. JOURNAL OF MAGNETIC RESONANCE IMAGING 2004; 19:800–815.

21. A De Roos, MD, et al. Cardiac applications of multislice computed tomography. The British Journal of Radiology, 79 (2006), 9–16.

22. KU Juergens, et al. Using ECG-Gated Multidetector CT to Evaluate Global Left Ventricular Myocardial Function in Patients with Coronary Artery Disease. AJR 2002;179:1545–1550.

23. MD Cerqueira, et al. American Heart Association Cardiac Imaging Committee of the Council on Clinical Cardiology of the Imaging of the Heart: A Statement for Healthcare Professionals From the Standardized Myocardial Segmentation and Nomenclature for Tomographic. Circulation 2002;105;539-542.

24. JD Schuijf, et al. Noninvasive Coronary Imaging and Assessment of Left Ventricular Function Using 16-Slice Computed Tomography. Am J Cardiol 2005;95:571–574.

25. KU Juergens, et al. Multi–Detector Row CT of Left Ventricular Function with Dedicated Analysis Software versus MR Imaging: Initial Experience. Radiology 2004; 230:403–410.

26. T Mochizuki, et al. Demonstration of Acute Myocardial Infarction by Subsecond Spiral Computed Tomography : Early Defect and Delayed Enhancement. Circulation 1999;99;2058-2059.

27. Jean-Franc¸ois Paul, et al. Late Defect on Delayed Contrast-enhanced Multi–Detector Row CT Scans in the Prediction of SPECT Infarct Size after Reperfused Acute Myocardial Infarction: Initial Experience. Radiology 2005; 236:485–489.

28. FYJ Keng. Clinical Applications of Positron Emission Tomography in Cardiology: A Review. Ann Acad Med Singapore 2004; 33: 175-82.

29. Josef Machac. Cardiac Positron Emission Tomography Imaging. Semin Nucl Med 35:17-36 © 2005

30. Josef Machac. PET Myocardial Perfusion Imaging. http://www.fac.org.ar/scvc/llave/image/machac/machaci.htm. Copyright© 1999-2001 Argentine Federation of Cardiology. 2nd Virtual Congress of Cardiology.

31. PG Camici. IMAGING TECHNIQUES: Positron emission tomography and myocardial imaging. Heart 2000;83;475-480.

32. S Hertel. PET Apps Cardiac. GE Healthcare, 2005.

33. R. Parkash. Potential utility of rubidium 82 PET quantification in patients with 3-vessel coronary artery disease. J Nucl Cardiol 2004;11:440-49.

34. G Germano, et al. Automatic Quantification of Ejection Fraction from Gated Myocardial Perfusion SPECT. J Nucl Med 1995; 36:2138-2147.

35. G Germano, et al. A New Algorithm for the Quantification of Myocardial Perfusion SPECT. I: Technical Principles and Reproducibility. J Nucl Med 2000; 41:712-719.

36. Langer and C Halldin. PET and SPET tracers for mapping the cardiac nervous system. Eur J Nucl Med 2002; 29: 416-434.

37. W Wijns. The Diagnosis of Coronary Artery Disease: In Search of a “One-Stop Shop”? J Nucl Med 2005; 46: 904.

38. M Schwaiger, S Ziegler and SG Nekolla. PET/CT: Challenge for Nuclear Cardiology. J Nucl Med 2005; 46: 1664-1677.

39. DE Mohrman, LJ Heller . Cardiovascular Physiology Fifth Edition. Lange Medical Books/McGraw-Hill. Copyright 2003. United States of America. The Electrocardiograph pgs 71-72.

40. The Basis of ECG Diagnosis. http://butler.cc.tut.fi/~malmivuo/bem/bembook/19/19.htm

41. G Ansalone, et al. Biventricular Pacing in Heart Failure: Back to Basics in the Pathophysiology of Left Bundle Branch Block to Reduce the Number of Nonresponders. Am J Cardiol 2003;91(suppl):55F–61F.

42. HJ Nesser, O-A Breithardt and BK Khandheria. Established and evolving indications for cardiac resynchronisation Heart 2004;90;5-9.

43. RN Doshi. Optimizing Resynchronization Therapy: Can We Increase the Number of True Responders? J Cardiovasc Electrophysiol, Vol. 16, pp. S48-S51, Suppl. 1, September 2005.

44. C-M YU, et al. Understanding Nonresponders of Cardiac Resynchronization Therapy—Current and Future Perspectives. J Cardiovasc Electrophysiol, 2005; 16: 1117-1124.

45. A Auricchio, et al. Effect of Pacing Chamber and Atrioventricular Delay on Acute Systolic Function of Paced Patients With Congestive Heart Failure. Circulation. 1999;99:2993-3001.

46. M Gasparini, et al. Is the Left Ventricular Lateral Wall the est Lead Implantation Site for Cardiac Resynchronization Therapy? PACE 2003; 26[Pt II]:162-168.

47. G Ansalone, et al. Doppler Myocardial Imaging to Evaluate the Effectiveness of Pacing Sites in Patients Receiving Biventricular Pacing. J Am Coll Cardiol 2002;39:489 –99.

48. G Ansalone, et al. Doppler myocardial imaging in patients with heart failure receiving biventricular pacing treatment. Am Heart J 2001;142:881-96.

49. SimpsonsRuleforAdditiveMethodofVolumeDetermination. http://depts.washington.edu/cvrtc/simplvgm.html. 1998-2004 University of Washington.

50. K Riouala, et al. MSCT labelling for pre-operative planning in cardiac resynchronization therapy Comp Med Img and Graph 29 (2005) 431–439.

51. M Gilard, et al. Multi-slice computer tomography of left ventricular function with automated analysis software in comparison with conventional ventriculography. European Journal of Radiology 59 (2006) 270–275. (40)

52. J Sra, G Narayan, D Krum, and M Akhtar. Registration of 3D computed tomographic images with interventional systems: Implications for catheter ablation of atrial fibrillation. J Interv Card Electrophysiol. DOI 10.1007/s10840-006-9030-8.

53. G. Ansalone, et al. “Biventricular Pacing in Heart Failure: Back to Basics in the Pathophysiology of Left Bundle Branch Block to Reduce the Number of Nonresponders”, Am J Cardiol vol. 91(suppl), pp. 55F-61F, 2003.

54. G. Ansalone, et al. “Doppler Myocardial Imaging to Evaluate the Effectiveness of Pacing Sites in Patients Receiving Biventricular Pacing”, J Am Coll Cardiol vol. 39, pp. 489-499, 2002.

55. P.W. Armstrong and GW Moe. Medical advances in the treatment of congestive heart failure. Circulation 1993;88;2941-2952.

56. R. Chandrashekara, R.H. Mohiaddin, and D. Rueckert. "Analysis of 3-D Myocardial Motion in Tagged MR Images Using Non-rigid Image Registration", IEEE Transaction on Medical Imaging vol. 23, pp. 1245-1250, 2004.

57. M.R. Cowie, et al. The epidemiology of heart failure. European Heart Journal (1997) 18, 208-225.

58. D. Farwell, NR Patel, A Hall, S Ralph and AN Sulke. How many people with heart failure are appropriate for biventricular resynchronization? European Heart Journal (2000) 21, 1246–1250.

59. LA Saxon and T De Marco. Cardiac Resynchronization: A Cornerstone in the Foundation of Device Therapy for Heart Failure*. Vol. 38, No. 7, 2001.

60. HJ Shenkman, et al. Congestive Heart Failure and QRS Duration: Establishing Prognosis Study. Chest 2002;122;528-534.

61. CM Yu, JJ Bax, M Monaghan and P Nihoyannopoulos. Echocardiographic evaluation of cardiac dyssynchrony for predicting a favourable response to cardiac resynchronisation therapy. Heart 2004;90;17-22.

62. R. Chandrashekara, R.H. Mohiaddin, and D. Rueckert. "Cardiac motion tracking in tagged MR images using a 4D b-spline motion model and non-rigid image registration", Biomedical Imaging: Nano to Macro, 2004. IEEE International Symposium on 15-18 April 2004, 468-471 Vol 1.

63. A. Rao, G.I. Sanchez-Ortiz, R. Chandrashekara, M. Lorenzo-Valdes, R.H. Mohiaddin, and D. Rueckert. "Comparison of cardiac motion across subjects using non-rigid registration", MICCAI 2002, LNCS 2488, pp. 722-729, 2002.

64. A. Rao, R. Chandrashekara, G.I. Sanchez-Ortiz , R.H. Mohiaddin, P. Aljabar, J.V. Hajnal, B.K. Puri, and D. Rueckert. "Spatial transformation of motion and deformation fields using non-rigid registration", IEEE Tras. Med. Img Volume 23 Issue 9 Sept 2004, 1065-1076.

65. J.V Hajnal, D.L.G. Hill, and D.J. Hawkes. Medical Image Registration. CRC Press LLC, Florida ISBN 0-8493-0064-9, pg 2001.

66. W.R. Crum, T. Hartkens, and D.L.G. Hill. Non-rigid image registration: theory and practice. The British Journal of Radiology, Special Issue 77 (2004), S140-S153.

67. Goshtasby A. Registration of images with geometric distortion. IEEE Trans. Geosci. Remote Sensing, 26, 60-64, 1988.

68. Rueckert D., Sonoda L.I., Hayes C., Hill D.L.G., Leach M.O. and Hawkes D.J. Non-rigid registration using free-form deformations: Application to breast MR images. IEEE Trans. Med. Imag., 18, 712–721, 1999.

69. Meyer C., Boes J., Kim B., Bland P., Zasadny P., Kison P., Koral K., Frey K. and Wahl R. (1997) Demonstration of accuracy and clinical versatility of mutual information for automatic multimodality image fusion using affine and thin-plate spline warped geometric deformations. Medical Image Analysis, 1, 195-207

70. M.H. Davis, A. Khotanzad, D.P. Flaming, and S.E. Harms. A physics-based coordinate transformation for 3-D image matching. IEEE Trans. Med. Imaging, 16(3):317-328, 1997.

71. Bajcsy R. and Kovacic S. (1989) Multiresolution elastic matching. Computer Vision, Graphics, and Image Processing, 46, 1-21.

72. A.F. Frangi, W.J. Niessen, and M.A. Viergever. Three-Dimensional modeling for functional analysis of cardiac images: A review. IEEE Trans. Med. Imaging 20(1):2-25, 2001.

73. H. Azhari, S. Sideman, J.L. Weiss, E.P. Shapiro, M.L. Weisfeldt, W.L. Graves, W.J. Rogers, and R. Beyar. "Three-dimensional mapping of acute ischemic regions using MRI: Wall thickening versus motion analysis," Amer. J. Physiol., pt.2, vol. 259, no. 5, pp. H1492-1503, Nov. 1990.

74. A. Suinesiaputra, A.F. Frangi, T.A.M. Kaandorp, H.J. Lamb, J.J. Bax, J.H.C. Reiber, and B.P.F. Lelieveldt. "Automated detection of regional wall motion abnormalities based on a statistical model applied to multislice short-axis cardiac MR images." IEEE Trans. Med. Imaging 28(4):595-607, 2009.

75. Bonneux L, Barendregt JJ, Meeter 1C, Bonsel GJ, van der Maas PJ. Estimating clinical morbidity due to ischemic heart disease and congestive heart failure: the future rise of heart failure. Am J Public Health 1994; 84- 20-8.

Appendix A – Example Code for Relative and Absolute Curve Calculation

```
clear all
close all

files = 'testfiles.dat'

%-----------------------------------------------------------
---------------
testfiles = textread(files,'%q');
numfiles = size(testfiles,1);
numphases = numfiles

phaserange = 1:numphases;

for incfile = 1:numfiles
    filename = char(testfiles(incfile));
    [cpgDisps(:,:,:,:,incfile) refpoints(:,:,incfile)
dimensions(:,:,:,incfile) affine(:,:,incfile)
affineparams(:,:,:,:,incfile) non-rigid(:,:,:,:,incfile)] =
loadreg(filename);
end

%-----------------------------------------------------------
---------------

%read in the diastole image for reference
I = analyze75read('phase0');

%Load the file that contains all of the points of interest
on the
%ventricle
load VentriclePointSelection.dat

%Determine how many points were found in the region of the
randomly selected point
F = size(VentriclePointSelection);
F = F(1)

fullXRange = -124.756:0.488281:124.756;%X Min/Max taken
from Origin in dof file, spacing taken from Spacing in dof
file
fullYRange = -124.756:0.488281:124.756;%Y Min/Max taken
from Origin in dof file, spacing taken from Spacing in dof
file
fullZRange = -75:1.25:75;
```

```
meshXRange = -141.39:8.31705:141.39;%Taken from Xmin, Xmax
and spacing in Bounds in dof file
meshYRange = -141.39:8.31705:141.39;%Taken from Ymin, Ymax
and spacing in Bounds in dof file
meshZRange = -92.6471:8.82353:92.6471;%Taken from Zmin,
Zmax and spacing in Bounds in dof file

%Now select the region of points that might be adjacent to
the randomly
%selected point
for W =1:F;
    nearX(W) = fullXRange(VentriclePointSelection(W,1));
    nearY(W) = fullYRange(VentriclePointSelection(W,2));
    nearZ(W) = fullZRange(VentriclePointSelection(W,3));
    [rX(W,:),cX(W,:),VX(W,:)] =
findnearest(nearX(W),meshXRange,0);
    [rY(W,:),cY(W,:),VY(W,:)] =
findnearest(nearY(W),meshYRange,0);
    [rZ(W,:),h(W,:),VZ(W,:)] =
findnearest(nearZ(W),meshZRange,0);
end

%Assume 9 phases, create X arrays for plotting motion, 1st
derivative, and
%2nd derivative
phases = size(testfiles,1);
X = 1:phases;
X2 = 1:phases+1;
X3 = 1:phases+2;

%Set kernels for 1st and 2nd derivatives
FirKernel = [1 -1];
SecKernel = [1 -2 1];

%Determine the motion plots for all points
for phases = 1:numphases
    for Q = 1:F
        Pointx_rel(Q,phases) = non-
rigid(cX(Q,1),cY(Q,1),h(Q,1),1,phases);
    end
end
for phases = 1:numphases
    for Q = 1:F
        Pointy_rel(Q,phases) = non-
rigid(cX(Q,1),cY(Q,1),h(Q,1),2,phases);
    end
end
```

```
for phases = 1:numphases
    for Q = 1:F
        Pointz_rel(Q,phases) = non-
rigid(cX(Q,1),cY(Q,1),h(Q,1),3,phases);
    end
end
%Determine the motion arrays for each point in the random
region
for phases = 1:2
    for Q = 1:F
        Pointx_abs(Q,1) = Pointx_rel(Q,1);
        Pointx_abs(Q,2) = Pointx_rel(Q,2) -
Pointx_rel(Q,1);

        Pointy_abs(Q,1) = Pointy_rel(Q,1);
        Pointy_abs(Q,2) = Pointy_rel(Q,2) -
Pointy_rel(Q,1);

        Pointz_abs(Q,1) = Pointz_rel(Q,1);
        Pointz_abs(Q,2) = Pointz_rel(Q,2) -
Pointz_rel(Q,1);
    end
end
for phases = 3:numphases
    for Q = 1:F
        Pointx_abs(Q,phases) = Pointx_rel(Q,phases) -
Pointx_abs(Q,phases-1);
        Pointy_abs(Q,phases) = Pointy_rel(Q,phases) -
Pointy_abs(Q,phases-1);
        Pointz_abs(Q,phases) = Pointz_rel(Q,phases) -
Pointz_abs(Q,phases-1);
    end
end

for phases = 1:numphases
    for Q = 1:F
        %Create a resultant from the x, y, and z components
of all of the dof files
        Point_rel(Q,phases) = sqrt((non-
rigid(cX(Q,1),cY(Q,1),h(Q,1),1, phases).^2) + (non-
rigid(cX(Q,1),cY(Q,1),h(Q,1),2, phases).^2) + (non-
rigid(cX(Q,1),cY(Q,1),h(Q,1),3,phases).^2));

        %Create a resultant from the x, y, and z components
of all of the dof files
```

```
        Point_abs(Q,phases) =
sqrt((Pointx_abs(Q,phases).^2) + (Pointy_abs(Q,phases).^2)
+ (Pointz_abs(Q,phases).^2));
    end
end

%Normalize the motion curves using sum of each motion curve
for Q=1:F
    Point_rel(Q,:) = Point_rel(Q,:)/sum(Point_rel(Q,:),2);
end

incinterp = 1;
interptype = 'cubic';
interprange = 1:incinterp:phases;
phaseinterprange = 5:incinterp:95;

%Up sample the motion plots to the specified increment
for Q=1:F
    PointUp_rel(Q,:) = interp1(X, Point_rel(Q,:),
interprange, interptype);
end

MeanMotionOfEachPhase = mean(PointUp_rel,1);

figure, plot(interprange,MeanMotionOfEachPhase,'ro-')
title('Relative Motion Curves')
xlabel('Time (Cardiac Phase)')
ylabel('Magnitude (mm)')
hold on
for Q=1:F
    plot(interprange,PointUp_rel(Q,:),'b.-')
end
plot(interprange,MeanMotionOfEachPhase,'ro-')

%Normalize the motion curves using sum of each motion curve
for Q=1:F
    Point_abs(Q,:) = Point_abs(Q,:)/sum(Point_abs(Q,:),2);
end

incinterp = 0.25;
interptype = 'cubic';
interprange = 1:incinterp:phases;

%Up sample the motion plots to the specified increment
for Q=1:F
    PointUp_abs(Q,:) = interp1(X, Point_abs(Q,:),
interprange, interptype);
```

```
end

MeanMotionOfEachPhase = mean(PointUp_abs,1);

figure, plot(interprange,MeanMotionOfEachPhase,'ro-')
title('Absolute Motion Curves')
xlabel('Time (Cardiac Phase)')
ylabel('Magnitude (mm)')
hold on
for Q=1:F
    plot(interprange,PointUp_abs(Q,:),'b.-')
end
plot(interprange,MeanMotionOfEachPhase,'ro-')
```